Earth Planet. Sci. Lett. 651 (2025) 119169

Contents lists available at ScienceDirect

Earth and Planetary Science Letters

journal homepage: www.elsevier.com/locate/epsl

Carbon, nitrogen, and noble gas isotopes reveal deep volatile signatures in thermal springs in the Central Volcanic Zone (CVZ) of the Andes

PH Barry [a,*], JM de Moor [b,c], MW Broadley [a,d], AM Seltzer [a], DV Bekaert [a,e], K Patil [a,f], CGE Bartels [a], ED Young [g], BE Longworth [a], B Barosa [a,h], A Bastianoni [h], D Bastoni [h], M Cascone [h], SJ Turner [i], RL Tyne [a,d], M Anderson [a], K Li [a], J Curtice [a], N Kumar [a], GL Jessen [j,k], JM Blamey [l], CJ Ramírez [m], A Chiodi [n], F Aguilera [o,p], S Layana [o], C González [o], M Aguilera [p,q], GPJ Masías Alvarez [r], B Marty [e], KG Lloyd [s], D Giovannelli [a,h,t,u,v,*]

[a] Woods Hole Oceanographic Institution, Woods Hole, MA, USA
[b] Observatorio Vulcanológico y Sismológico de Costa Rica (OVSICORI), Universidad Nacional, San Jose, Costa Rica
[c] University of New Mexico, Albuquerque, NM, USA
[d] Department of Earth and Environmental Science, University of Manchester, Manchester, UK
[e] Université de Lorraine, CNRS, CRPG, 54000 Nancy, France
[f] Brown University, Providence RI, USA
[g] University of California Los Angeles, Los Angeles CA, USA
[h] Department of Biology, University of Naples "Federico II", Naples, Italy
[i] University of Houston, Houston, TX, USA
[j] Instituto de Ciencias Marinas y Limnológicas, Universidad Austral de Chile, Valdivia, Chile
[k] Centro de Investigación Oceanográfica COPAS Coastal, Universidad de Concepción, Concepción, Chile
[l] Fundación Biociencia, Universidad de Santiago de Chile, Santiago, Chile
[m] Servicio Geológico Ambiental (SeGeoAm), Heredia, Costa Rica
[n] Instituto de Bio y Geociencias del NOA (IBIGEO, UNSa-CONICET), Salta, Argentina
[o] Millennium Institute on Volcanic Risk Research - Ckelar Volcanoes, Antofagasta, Chile
[p] Departamento de Ciencias Geológicas, Universidad Católica del Norte, Antofagasta, Chile
[q] Programa de Doctorado en Ciencias mención Geologia, Universidad Católica del Norte, Antofagasta, Chile
[r] Instituto Geológico Minero y Metalúrgico (INGEMMET), Arequipa, Perú
[s] University of Southern California, Los Angeles CA, USA
[t] Earth-Life Science Institute, Tokyo Institute of Technology, Tokyo, Japan
[u] National Research Council, Institute of Marine Biological Resources and Biotechnologies—CNR-IRBIM, Ancona, Italy
[v] Department of Marine and Coastal Science, Rutgers University, New Brunswick, NJ, USA

ARTICLE INFO

Editor: Dr R. Hickey-Vargas

Keywords:
Subduction zones
Noble gases
Nitrogen
Carbon
Radiocarbon
Volatiles

ABSTRACT

In subduction zones, thermal springs release deeply-sourced volatiles from Earth's mantle, crust, and/or subducted slab-derived material. The origin and apparent ages of these volatiles are important for understanding the deep volatile cycle, which in turn affects the distribution of microbial life in the subsurface. Here, we report carbon (^{13}C, ^{14}C), noble gas (He, Ne, Ar, Kr and Xe), and clumped nitrogen isotope data in gas and water samples from thermal springs within the Central Volcanic Zone (CVZ) of the Andean Convergent Margin (ACM). He isotopes show that CVZ gases are predominantly sourced from the crust (~77 %), with smaller mantle contributions (~23 %), consistent with previous studies from the CVZ. Thermal spring samples with non-atmospheric He-Ne characteristics have low ^{14}C activities, and are deeply derived (i.e., from the mantle and crust) and old (>22,000 years). To gain additional constraints on volatile sources, a gas sample from Pirquitas Argentina was analyzed using a new high-precision technique to reveal significant geogenic anomalies in argon ($^{40}Ar/^{36}Ar$ = 492), fissiogenic xenon (88 % crustal), and helium (84 % crustal) isotopes. Clumped N_2 isotopologue results also indicate that the N_2-rich Pirquitas sample is dominated by crustal and magmatic N_2, which was unambiguously released at high temperatures (indicated by Δ_{30} of ~0‰). When taken together, all carbon, noble gas and

* Corresponding authors.
E-mail address: pbarry@whoi.edu (P. Barry).

https://doi.org/10.1016/j.epsl.2024.119169
Received 5 September 2024; Received in revised form 13 November 2024; Accepted 7 December 2024
Available online 21 December 2024

clumped N_2 isotope data from CVZ thermal springs point toward a predominantly crustal source of volatile elements, which is consistent with the thick crust beneath the arc. We conclude that thermal springs with noble gas isotopic evidence for minimal air contributions are old, suggesting that any microbial communities entrained in them are also supported by deeply-derived and old organic carbon.

1. Introduction

In subduction zone settings, deeply-sourced volatile elements (e.g., carbon, noble gases, nitrogen) are primarily derived from Earth's mantle, crust, and/or subducted slab-derived material (e.g., Hilton et al., 1993; 2002; Barry et al., 2019). Mafic lavas and high temperature fumarolic gases are typically considered the best archives of deep volatile sources. However, eruptive materials are not always accessible and volcanic summits are often difficult (or impossible) to reach. Warm and hot "thermal springs" are generally easier to access, and He-C isotopes from such samples often reveal vital information about deeply-sourced volatiles as well as processes occurring deep within Earth's crust (e.g., Ray et al., 2009; Barry et al., 2022). For example, helium isotopes ($^3He/^4He$) and $^4He/^{20}Ne$ values have been used to show the extent of mixing with air components, and $CO_2/^3He$ and $\delta^{13}C$ have been extensively utilized to estimate mantle vs slab contributions to volcanic and thermal manifestations (Sano and Marty, 1995). Furthermore, interpreting noble gases alongside ^{14}C data can provide information about the duration of time that subsurface fluids have been isolated from surface reservoirs (e.g., radiocarbon-dead samples imply apparent ages >40,000 (Stuiver and Polach, 1977; Mook and Van Der Plicht, 1999)). Measurement of low ^{14}C activity provides confidence that samples are deeply-derived and have not extensively mixed with surface-equilibrated fluids. Using such a multipronged isotope approach allows for the deconvolution of deep and shallow source signals, which is critical for robust interpretations of volatile sources from thermal springs in subduction zone settings.

Understanding volatile sources is also important for geomicrobiology, as Earth's crust is home to a sizable microbial ecosystem (Kallmeyer et al., 2012; Magnabosco et al., 2018), sustained by deeply-sourced volatiles (Fullerton et al., 2021). In turn, the subsurface microbial biosphere plays a crucial role in regulating global biogeochemical cycles by influencing the subsurface redox state and can be used to determine the distribution of minerals, gases, and organic matter within the crust (D'Hondt et al., 2019). Despite their significance in surface geological processes and the cycling of volatiles throughout deep time, we know far less about subsurface microbial ecosystems than those at the surface. This knowledge gap primarily stems from the challenges of accessing deep subsurface environments. Typically, direct access to the subsurface microbiome is achieved through scientific drilling programs, which have provided unprecedented opportunities to explore subsurface fluids and their accompanying ecosystems. However, deep drilling projects are costly and infrequent (Orcutt and Edwards, 2014). An alternative, and potentially fruitful approach to studying the deep subsurface biosphere is through thermal features (i.e., springs) that are thought to be deeply-sourced (Summit and Baross 2001). Therefore, a

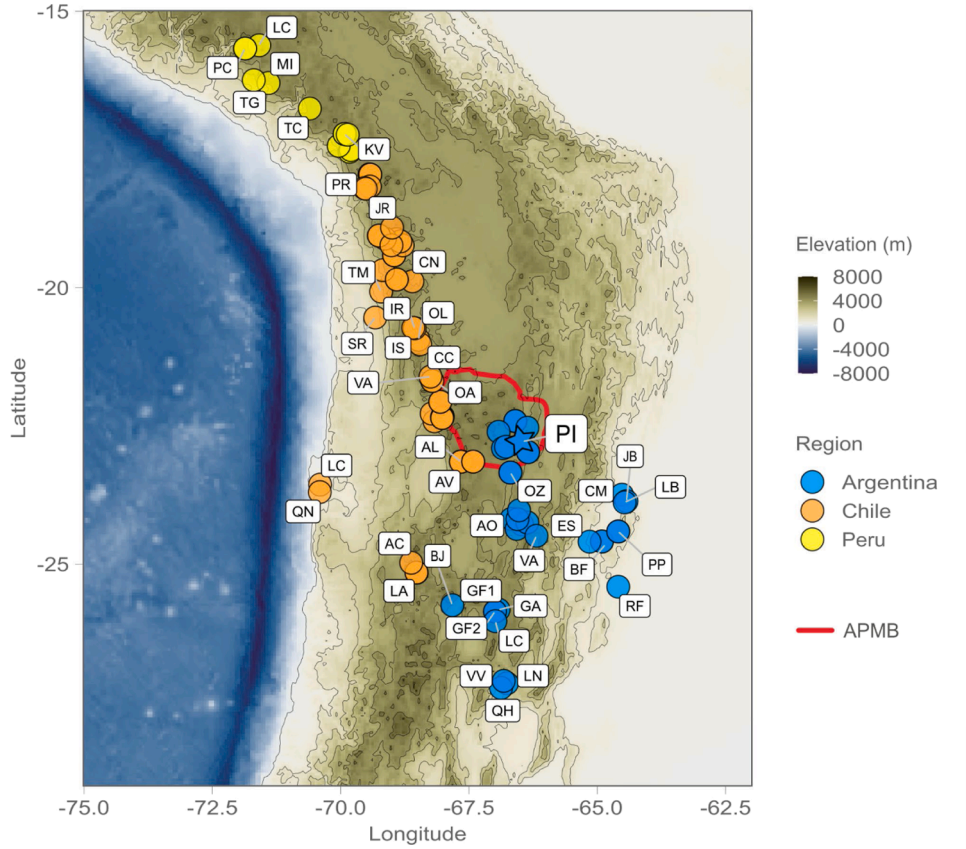

Fig. 1. Map showing sample localities throughout the CVZ. The two letter sample ID corresponds to the sample IDs in the tables. Topography is shown as elevation in meters above mean sea level (MAMSL). The location of the Altiplano Puna Magma Body (APMB) is shown as a red outline (Perkins et al., 2016). As in all figures, the star symbol is used to denote gas phase sample PI230308 from Piquiras, as this sample was targeted for high precision Ar, Kr, Xe and clumped N_2 measurements.

deeper look at the noble gas, carbon and nitrogen isotopic systems is crucial for determining whether such thermal springs can be used to passively sample subsurface microbial communities, massively expanding our ability to sample such ecosystems beyond the small number of locations accessible by drilling.

Here, we present new $\delta^{13}C$, ^{14}C, noble gas (He, Ne, Ar, Kr, Xe), $\delta^{15}N$ and clumped N_2 isotope data from natural springs in the Central Volcanic Zone (CVZ) of the Andean Convergent Margin (ACM) (Fig. 1; Tables 1–5). These data are used to determine 1) the time since fluids were exposed to surface reservoirs, and 2) the origin (mantle and crustal) of non-surface derived volatiles. In this way, we can investigate the interplay between subsurface and surface processes, providing insights into large scale geological processes such as the deep volatile recycling budget. Furthermore, these data will provide important context for future subsurface biological studies that aim to assess microbial community structure and function of microbial populations.

2. Geological setting

The ACM consists of more than 200 Quaternary volcanoes and twelve large caldera/ignimbrite systems formed by the subduction of the Nazca Plate beneath South America (e.g., Stern, 2004). Volcanism is distributed across four distinct segments: the Northern Volcanic Zone (12°N-5°S), Central Volcanic Zone (5–33°S), Southern Volcanic Zone (33–49°S), and Austral Volcanic Zone (49–56°S) (Stern, 2004). The young (32 Ma) Nazca plate subducts beneath the CVZ at a shallow angle (27°) with a convergence rate of 74 km/Ma, and carries a thinner sediment layer compared to the Southern margin (Syracuse and Abers, 2006; Clift, 2017; Lages et al., 2021).

The CVZ is home to 62 (potentially) active volcanoes (de Silva and Francis, 1991; Aguilera et al., 2022), and is built on the thickest crust (60–70 km) of any volcanic arc on Earth (McGlashan et al., 2008; Profeta et al., 2015). Volcanic materials consist mostly of andesites and dacites. Hydrothermal activity occurs throughout the CVZ, observed in geothermal fields and thermal springs. Beginning at 38 Ma, the region from 14 to 20°S experienced a flat slab subduction event, leading to a cessation of magmatism at the prior arc front location and an eastward migration of volcanism (Ramos and Folguera, 2008). The region of flat subduction (and cessation of volcanism) then progressed southward towards 20–24°S from 18 to 12 Ma, which may have led to hydration or alteration of the lower crustal region (Newell et al., 2015).

Around 11 Ma, large ignimbrite complexes were formed over the Altiplano-Puna Volcanic Complex (APVC) within the CVZ, many of which retain a well-mixed crustal-mantle signature, indicating large amounts of mixing deep within the crust (Kay et al., 2009; de Silva et al., 2006; Salisbury, 2011; de Silva and Kay, 2018). Notably, the Altiplano-Puna Magma Body (APMB) is located approximately 10–20 km beneath the APVC (Fig. 1). High resolution tomography shows that this magma body has a diameter of ~200 km and a total volume of ~500,000 km^3 (e.g., Ward et al., 2014) making it the largest known active magma body on Earth (Perkins et al., 2016). However, the CVZ crust over the APMB remains thickened (Perkins et al., 2016). The complex interplay between the thick crust and the APMB likely impacts the geochemical signatures of emitted volatiles, however this remains poorly understood.

3. Results and discussion

He and C isotopes are often considered to be the 'gold standard' of tracers for deep volcanically derived source features, because geogenic He and C isotopic signals are often very clearly identifiable. However, detecting meaningful geothermal signals from isotopes of the heavier noble gases (Ne, Ar, Kr and Xe) and N isotopes is more challenging for two reasons. First, there is a large discrepancy between these two groups of elements (i.e., He/C vs Ne/Ar/Kr/Xe/N) in terms of mass balance considerations in gas and water systems. Namely, the amount of He and C emanating from deep reservoirs far outweighs surface (i.e., atmospheric) inputs of He and C in volcanically active geothermal systems. In contrast, Ne, Ar, Kr, Xe and N are found in trace amounts in the mantle and crust, relative to their atmospheric abundances (e.g., Butler et al., 1963). Second, mantle and crustal isotope endmembers for Ne, Kr, Xe, and N closely resemble the atmospheric composition, unlike He and C, therefore making it difficult to resolve deep geothermal anomalies from atmospheric signals. As a result, heavy noble gases have seldom been reported or exploited in volcanic settings, whereas He-C systematics have been used extensively (e.g., Hilton et al., 1993; Ray et al., 2009; Barry et al., 2013; 2019; 2022; Bekaert et al., 2021).

Below we discuss new He-C results alongside radiocarbon activity data, which clearly show that these tracers are robust indicators of old (i.e., >22,000 year) and deep (mantle and crustal) sources. We also present Ne, Ar and Xe data from a subset of samples, along with high precision Xe and clumped N_2 data for a single sample. All noble gas and stable isotope results are detailed in Tables 2–5. The single "case-study" sample (i.e., Pirquitas; PI230308) has a large Ar isotope anomaly ($^{40}Ar/^{36}Ar > 463$), which is significantly higher than air, suggesting that Pirquitas retains a deep signature despite overwhelming atmospheric heavy noble gas contents in the system. Using a recently developed high precision technique, enabled by dynamic mass spectrometry (e.g., Seltzer and Bekaert, 2022), we show that high-precision Xe isotopes can be used to resolve small, yet significant, deep geogenic signals that provide important information about the extent of mantle and crust feeding Pirquitas. Furthermore, the Pirquitas sample was analyzed for clumped N_2 isotopes, which confirms that atmosphere-derived N_2 is completely overprinted by N_2 of a high-temperature origin, as is evidenced by high N_2/Ar and non-atmospheric Δ_{30} values (see Section 3.6). This finding is intriguing because it unambiguously indicates crust-mantle interaction occurring at high temperatures in the subsurface.

3.1. Data integrity

In Fig. 2 we plot $^3He/^4He$ vs $^4He/^{20}Ne$ for all gas and water samples, along with "air". Mixing lines are also shown to indicate mixing between "air" (or air saturated water) and deep mantle and crustal endmembers. We show that the vast majority of samples have $^4He/^{20}Ne$ values >2, strongly suggesting a deep (crust + mantle) He source. Data are consistent with those previously published from the CVZ (e.g., Lages et al., 2021; Barry et al., 2022 and references within). Due to the deep source of He, it has long been asserted that C is also deeply derived, as it is the major volatile (along with water) in volcanic gases and the likely carrier of noble gases and other trace volatile elements in volcanically influenced thermal spring samples. For CVZ gas and water samples, this assertion is broadly consistent with $CO_2/^3He$ and ^{13}C isotopes, which also suggest deep (i.e., mantle or crustal derived C sources). For example, in Fig. 3 the majority of samples plot inside a three component mixing envelope defined by mantle and slab derived (sediment and limestone) endmembers (Sano and Marty, 1995). For reference, "air" has a $\delta^{13}C$ of ~−8‰ vs. PDVB and a $CO_2/^3He$ of $\sim 6 \times 10^7$, which plots distinctly below the envelope defined by mantle and slab mixing.

3.2. Bimodal ^{14}C signals: deep and "dead" vs. shallow and "active"

We also report radiocarbon (^{14}C) activities of dissolved inorganic carbon (DIC) with fraction modern ($F^{14}C$) between 0 (i.e., below the detection limit) and 0.84, corresponding to apparent groundwater residence times of between >41,100 and 1380 years in water samples from the CVZ. These data are presented along with noble gases and $\delta^{13}C$ of DIC and gaseous $\delta^{13}C$ of CO_2 from thermal springs in the CVZ. We show a striking relationship between radiocarbon activities (F Modern DIC), $^3He/^4He$ (Fig. 4a) and $^4He/^{20}Ne$ (Fig. 4b). Every sample with non-atmospheric He-Ne signature (i.e., $^3He/^4He > 1.8\ R_A$ and $^4He/^{20}Ne > 2$) is also essentially radiocarbon dead (i.e., $F^{14}C < 0.07$). This implies that

Table 1
Meta data for all localities sampled, including latitude, longitude, elevation, temperature and pH of the thermal springs. Temperatures are given in Celsius and elevations are in meters above sea level. Measurements were made in the field.

Region	Name	Site ID	Lat	Long	Elev	T (°C)	pH
Chile	La Chimba	LC220316	−23.5629	−70.40019	13	40.3	7.34
Chile	Quebrada Negra	QN220317	−23.69785	−70.40637	94	26.4	7.11
Chile	El Chitór	CH220319	−22.41729	−68.1726	3754	21.7	5.77
Chile	Rio Salado	RS220319	−22.27811	−68.22771	3084	22.24	6.01
Chile	Alitar fumaroles	AL220320	−23.14591	−67.65525	4747	82.5	NA
Chile	Alitar fumaroles	AL230302	−23.14588	67.65518	4740	85.1	NA
Chile	Alitar verde	AV220320	−23.14915	−67.65849	4705	68.2	5.95
Chile	Laguna Negra	LN220321	−23.14677	−67.41922	4227	52.3	6.58
Chile	El Tatio_Bubbling pool	ET220322	−22.33071	−68.01182	4278	86.8	6.31
Chile	El Tatio_River	ET220322R	−22.34071	−68.02614	4237	NA	NA
Chile	Geyser Blanco	GB220322	−22.35696	−68.02258	4287	83.1	6.58
Chile	Cabana	CA220323	−22.06502	−68.05921	4061	25	7.36
Chile	Olca Volcano_Fum1	OL220324	−20.9412	−68.48334	5312	147.1	NA
Chile	Vega Churchilla	CC220324	−21.02515	−68.45084	4266	20.3	7.85
Chile	Carcote	CR220324	−22.06499	−68.05932	4125	42.2	7.92
Chile	Ojo de Ascotán vertiente 11	OA220325	−21.6879	−68.21487	3736	27.5	6.96
Chile	Vertiente 10 Ascotán	VA220325	−21.60952	−68.25012	3795	22.2	7.15
Chile	Termales Mamiña	TM220326	−20.07042	−69.21176	2804	53.9	8.84
Chile	Termales Cancosa	CN220327	−19.88536	−68.6013	3906	37.2	6.23
Chile	Termales Lirima	LR220327	−19.85184	−68.90653	3999	68.7	6.28
Chile	Irruputuncu fumaroles	IR220328	−20.73451	−68.55741	4977	408	1.24
Chile	Irruputuncu acid spring	IS220328	−20.72589	−68.58618	4042	38.41	2.38
Chile	Santa Rosita	SR220328	−20.54046	−69.32597	1322	34.8	8.26
Chile	Termales Chusmiza	CZ220329	−19.68348	−69.17722	3423	41.7	8.2
Chile	Puchuldiza outflow	PZ220330	−19.40849	−68.95853	4205	74	7.17
Chile	Puchuldiza outflow_pool2	PZ220330	−19.40849	−68.95853	4205	NA	NA
Chile	Puchuldiza fumarole	PD220330	−19.41281	−68.95793	4222	85.9	7.1
Chile	Puchuldiza boiling pool	PD220330	−19.41281	−68.95793	4222	85.1	8.02
Chile	Parajaya	PJ220330	−19.12084	−68.90981	4242	29.6	6.74
Chile	Termales Enquelga	EQ220330	−19.23506	−68.79199	3901	30.1	6.02
Chile	Isluga volcano	IV220331	−19.16223	−68.83487	5163	97	1.29
Chile	Termal Tana	TT220331	−19.11342	−69.13836	4067	66.6	6.31
Chile	Laguna Amarilla	LA220331	−19.05879	−69.25277	3728	35.5	6.77
Chile	Laguna Roja	LR220331	−19.85176	−68.90614	4079	24.3	5.5
Chile	Laguna Verde	LV220331	−19.05701	−69.2534	3731	49.1	5.6
Chile	Laguna Parinacota	LP220401	−19.23299	−69.0104	4157	24.9	7.45
Chile	Baño Polio Quieres (?) Salar Surire	PQ220401	−18.91319	−68.99922	4283	63.4	5.75
Chile	Colpitas	CP220402	−17.95005	−69.43621	4151	16	3.81
Chile	Colpitas East	CE220402	−17.95554	−69.42357	4141	53.5	6.19
Chile	Las Cuevas	CU220402	−18.16997	−69.43094	4473	33.7	6.44
Chile	Putre	PR220403	−18.19791	−69.53851	3785	35.8	6.33
Chile	Termales Jurasi	JR220403	−18.2102	−69.51053	4050	65.4	6.9
Chile	Lastarria volcano_Fum1	LA220409	−25.15544	−68.51953	5124	230	1.22
Chile	Lastarria volcano_Fum2	LA220409	−25.1527	−68.52339	4966	310	1.12
Chile	Salar Aguas Calientes	AC220410	−24.97643	−68.62558	3675	24.4	6.85
Peru	La Calera	LCL221109	−15.61489	−71.58689	3620	68.2	6.3
Peru	Pinchollo_boiling pool	PC221110	−15.67377	−71.86186	4363	85	6.05
Peru	Pinchollo_fumarole	PC221110C	−15.67377	−71.86186	4363	86.6	6.25
Peru	Ticsani	TC221112(1)C	−16.75915	−70.60103	5315	80.8	4.3
Peru	Misti	MI221116C	−16.2976	−71.40578	5585	255	1.58
Peru	Llavemoco	LL221118C	−17.54163	−69.82695	4862	86	5.84
Peru	Casiri	CA221118	−17.50861	−69.80222	4616	47.8	6.36
Peru	Putina	PT221119	−17.43421	−70.03834	3314	50.3	7.51
Peru	Kovire	KV221120	−17.21906	−69.92208	4381	86.4	7.65
Peru	Kovire	KV221120C	−17.21906	−69.92208	4381	86.4	7.3
Peru	Calachaca	CL221120	−17.23272	−69.8628	4298	45.6	6.59
Peru	El Tigre/Yura	TG221122	−16.24527	−71.69355	2519	32.6	6.13
Argentina	Banos Fleming	BF230316	−24.59134	−64.91012	595	29.15	7.66
Argentina	Botijuela	BJ190227	−25.74303	−67.82325	3524	40	6.44
Argentina	Caimancito	CM230315	−23.74437	−64.51974	385	56.6	8.26
Argentina	Coranzuli	CZ230307	−22.97502	−66.3491	4148	33.53	7.48
Argentina	El Sauce	ES230304	−24.59445	−65.15059	838	35.18	6.8
Argentina	Galán Aguas Calientes	GA190226	−25.82542	−66.9225	4482	67	6.7
Argentina	Galán Fumaroles	GF190226_1	−25.85819	−66.9927	4644	80	7.75
Argentina	Galán Fumaroles	GF190226_2	−25.85824	−66.99282	4651	80	3.21
Argentina	Incachule	IN190223	−24.28213	−66.46676	4470	46.9	6.52
Argentina	Well YPF JB5	JB230315	−23.86217	−64.43037	560	71.5	7.2
Argentina	Laguna La Brea	LB230315	−23.88503	−64.46661	635	59.4	6.32
Argentina	Galán La Colcha	LC190226	−26.03291	−66.98609	4728	84	6.94
Argentina	Lagunilla del Farallon	LF230308	−22.41294	−66.59731	3890	53.7	6.51
Argentina	Los Nacimientos	LN230313	−27.15565	−66.75972	2097	38.52	6.55
Argentina	Laguna de Vilama	LV230309	−22.60727	−66.92273	4489	30.2	5.96
Argentina	Orosmayo	OY230308	−22.53242	−66.36244	3996	25.39	8.04

(*continued on next page*)

Table 1 (*continued*)

Region	Name	Site ID	Lat	Long	Elev	T (°C)	pH
Argentina	Olaruz	OZ230305	−23.34416	−66.69222	3939	14.4	6.2
Argentina	Pastos Grandes	PG290225	−24.36459	−66.57113	4305	44.9	8.74
Argentina	Pirquitas	PI230308	−22.73454	−66.46609	4105	23.35	6.34
Argentina	Pompeya	PM190223	−24.24669	−66.36272	3889	50.3	6.53
Argentina	El Galpón	PP190301	−24.40986	−64.59146	493	54.3	8.47
Argentina	Pairique	PQ230306	−22.9028	−66.8383	4292	43.35	7.16
Argentina	Quebrada de Hualfil	QH230313	−27.24069	−66.87535	1847	37.18	8.94
Argentina	Rosario de Coyaguima	RC1230306	−22.87706	−66.77885	4328	55.6	6.61
Argentina	Rosario de la Frontera	RF190301	−25.40986	−64.59134	425	82	8.23
Argentina	Tocomar	TM190224	−24.18778	−66.55451	4333	69.2	7.13
Argentina	Termas de Tuzgle	TZ230310	−24.02815	−66.52361	4213	55.6	6.27
Argentina	Vega Acida	VA230311	−24.48921	−66.18411	3918	15.58	3.95
Argentina	Villa Vil	VV190228	−27.11286	−66.82224	2143	38.2	9.09

any sample with non-atmospheric He-Ne characteristics is derived from a deep carbon pool that has not equilibrated with air for at least ~22,000 years. However, apparent ages in hydrothermal fluids are fundamentally uncertain and it is important to point out that low radiocarbon activities may reflect the addition of dead magmatic C and may not truly reflect time elapsed since exposure to the atmosphere. This is because radiocarbon activities are not solely representative of the atmospheric value, but instead a complex function of the mass ratio of atmospheric C and alkalinity-related carbonate. For this reason, apparent ages should be considered maximum estimates, because if the carbon pool is in fact dominated by deep, dead mantle carbon, waters could be younger than they appear. Nonetheless, these findings indicate that volatiles in these thermal spring samples are unequivocally old and deeply derived. Notably, the bimodal distribution between radiocarbon-active and old water samples is more readily apparent when plotted vs. He-Ne systematics than it is versus other (first order) indicators of depth, such as temperature (Fig. 4c) and pH (Fig. 4d). This indicates that He isotope and $^{4}He/^{20}Ne$ signatures are more faithful proxies for sample age and source/depth than temperature and pH, which can be more easily influenced by shallower factors, such as flow rates or local lithology.

In order to contextualize the importance of these findings, we note that in previous He-C studies in volcanic regions (e.g., Barry et al., 2019) the origin of carbon was essential to the broader interpretation of how volatiles move through subduction zone systems. For instance, isotopically light $\delta^{13}C$ of DIC could either be interpreted as being surface-derived (i.e., decay of organic material in the vicinity of the springs) or resulting from isotopic fractionation at depth. This has important implications for reconstructing the history of volatile cycling between surface reservoirs (i.e., atmosphere, ocean, crust) and for identifying potentially important carbon sinks in Earth's crust. There are also important ramifications for microbiological interpretations, as Earth's crust is home to a sizeable microbial ecosystem (Kallmeyer et al., 2012; Magnabosco et al., 2018) much of which may be sustained by deeply-derived volatile elements such as H, C and S (Fullerton et al., 2021) used by microorganisms as energy sources (Hay Mele et al., 2023). Determining the source (deep vs shallow, magmatic vs crustal, old vs young/surface derived) of the volatiles feeding the microorganisms in the deep subsurface is thus critically important, because the deep microbial biosphere plays a potentially important role in regulating global biogeochemical cycles (Giovannelli, 2023) by influencing the redox state of the crust and determining the redistribution of minerals, gases, and organic matter transformations (D'Hondt et al., 2019). These results support the idea that thermal springs with noble gas isotopic evidence for minimal air contributions can be considered windows into the subsurface (Giovannelli et al., 2022), and are indeed deeply-derived. As a result, microbiological communities that are flushed to the surface at thermal springs can be sampled to investigate the interactions of the community with geothermal waters that are replete with ancient carbon derived from deep within the crust and/or mantle. Noble gas systematics are thus an attractive way to determine which natural springs can be used as passive sampling ports for subsurface ecosystems, without requiring deep drilling of boreholes to access them (Giovannelli et al., 2022).

These new radiocarbon activity findings thus confirm that carbon in samples with deeply-derived (i.e., non-atmospheric) He-Ne, is deeply sourced, confirming biological interpretations of deep signals based off of He isotopes (Fullerton et al., 2021; Rogers et al., 2023; Basili et al. 2024). Traditionally, high-temperature fluids were considered most representative of the deep subsurface. Our findings open the possibility of also considering lower-temperature fluids to study deep volatiles, greatly expanding the locations that can be sampled.

3.3. Volatile sources

3.3.1. Helium

Helium isotope results ($^{3}He/^{4}He$ of sample = R) are reported relative to air (R_A), corrected for the occurrence of atmospheric He (to R_C/R_A) and blank contributions, which are consistently less than 5 %. The $^{4}He/^{20}Ne$ value (Tables 2 and 3) is used to apply an atmospheric correction to all samples, assuming ^{20}Ne is derived from air ($^{4}He/^{20}Ne$ = 0.32) or fresh air saturated water ($^{4}He/^{20}Ne$ = 0.26 at 15 °C; Hilton, 1996; Ozima and Podosek, 2002). Uncorrected helium isotopes range from 0.4 to 5.6 R_A in gas samples and 0.1 to 3.5 R_A in water samples. When the $^{3}He/^{4}He$ is corrected (using methods of Hilton, 1996), the highest $^{3}He/^{4}He$ values found are 5.8 R_A in gas samples and 4.4 R_A in water samples, which is consistent with previous findings (e.g., Lages et al., 2021; Barry et al., 2022). Barry et al. (2022) showed that $^{3}He/^{4}He$ values in thermal springs range from 0.1 R_A to 2.6 R_A, and are slightly lower (more radiogenic) than recent reports of He isotopes from waters and gases within the region (which range from 0.1 R_A to 5.5 R_A; e.g., Lages et al., 2021). These findings suggest overprinting by crustal signatures throughout the CVZ (Fig. 2), which is broadly consistent with the thick crust found throughout the CVZ. Notably, however, high temperature CVZ volcanic gas samples have $^{3}He/^{4}He$ values (Barry et al., 2022; de Moor et al., In Review) approaching the arc endmember value of ~5.4 ± 1.9 R_A (Hilton et al., 2002).

Helium can be derived from the mantle, crust, and/or atmosphere, and the relative contributions of these different sources will ultimately control the $^{3}He/^{4}He$ of a given sample. The average air corrected He isotopes value reported here is 1.9 R_A. Using the methods of Barry et al. (2013) we calculate that the CVZ is characterized by 23 % mantle He and 77 % crustal He on average, which is nearly identical to previous findings from the area (Barry et al., 2022), despite the samples being collected at different locations. The extent of mixing between crustal and mantle components is considered to be controlled by the thickness of the crust (e.g., Barry et al., 2022). We note that in the CVZ, where the crust is ~70 km thick on average, the mean $^{3}He/^{4}He$ is lower (R_C/R_A = 1.9 R_A) than in other parts of the ACM as well as in other subduction zones globally (Hilton et al., 2002). As hydrothermal fluids migrate through thicker sections of crust in the overriding plate, they incorporate radiogenic ^{4}He due to interaction with the U- and Th-rich country

Table 2
Noble gas isotope and carbon isotope data for gas phase samples. Uncertainties are less than 5 % for all isotopes, concentrations, and elemental ratio reported. Noble gas data were acquired by static mass spectrometer in the Barry Lab at WHOI. Carbon (13C) measurements were done at OVSICORI.

Region	Site ID	$^{3}He/^{4}He$ R/RA	$^{4}He/^{20}Ne$	$^{3}He/^{4}He$ RC/RA	$CO_2/^{3}He$	$^{20}Ne/^{22}Ne$	$^{21}Ne/^{22}Ne$	$^{40}Ar/^{36}Ar$	^{4}He (cm3STP/cm3)	^{20}Ne (cm3STP/cm3)	^{36}Ar (cm3STP/cm3)	CO_2	He	$\delta^{13}C$ CO_2 vs PDB
Chile	CH220319	1.03	0.33	1.89	8.77E+10				4.38E-06	1.34E-05		94.7 %	0.00076 %	−6.6
Chile	RS220319	0.99	0.29	1.13	1.57E+10				4.33E-06	1.47E-05		93.8 %	0.00434 %	−5.5
Chile	AL220320	3.16	11,498.43	3.16	2.14E+10				2.92E-06	2.54E-10		0.4 %	0.00000 %	−10.6
Chile	AV220320	3.28	65.56	3.29	6.04E+10				7.99E-07	1.22E-08		99.4 %	0.00036 %	−8.7
Chile	LN220321	1.83	45.10	1.84	2.82E+09				2.86E-04	6.33E-06		72.1 %	0.01005 %	−12.2
Chile	OL220324	1.71	12.63	1.72	3.00E+10				2.33E-06	1.84E-07		0.7 %	0.00001 %	−4.8
Chile	OA220325	0.99	1.45	0.98	7.33E+09				8.31E-06	5.71E-06		17.5 %	0.00174 %	−9.3
Chile	CN220327	1.03	0.29	0.68	6.65E+11				4.07E-06	1.38E-05		99.8 %	0.00011 %	−6.9
Chile	LR220327	1.05	0.29	0.53	9.31E+8				4.25E-06	1.48E-05		48.4 %	0.03563 %	−3.6
Chile	IR220328	5.59	7.56	5.79	2.99E+10				6.72E-07	8.89E-08		3.1 %	0.00001 %	−5.4
Chile	PZ220330	1.91	12.97	1.93	2.05E+10				1.13E-05	8.69E-07		95.3 %	0.00175 %	−4.9
Chile	PD220330	1.66	1653.06	1.66					6.16E-07	3.73E-10				
Chile	IV220331	4.46	35.75	4.49	6.01E+10				1.36E-06	3.79E-08		2.5 %	0.00001 %	−6.2
Chile	LA220331	2.29	101.52	2.29					5.24E-05	5.16E-07				
Chile	LV220331	2.20	29.93	2.21	1.93E+10				1.23E-05	4.10E-07		96.3 %	0.00163 %	
Chile	CE220402	1.71	41.93	1.72					6.14E-08	1.46E-09		99.9 %		−7.0
Chile	CU220402	1.22	25.35	1.22					8.08E-05	3.19E-06				
Chile	LA220409	5.35	4172.62	5.35	7.46E+9				3.46E-06	8.30E-10		4.1 %	0.00007 %	−3.3
Peru	LCL221109	1.53	786.30	1.53	5.75E+09	9.65	0.03	311.63	1.18E-05	1.50E-08	9.79E-08	96.8 %	0.00792 %	−8.5
Peru	PC221110	1.35	567.18	1.35	2.29E+09	9.88	0.03	325.50	4.48E-04	7.89E-07	3.92E-06	0.9 %	0.00020 %	−6.3
Peru	PC221110C	1.36	234.85	1.36	1.37E+10	10.03	0.03	316.14	7.42E-06	3.16E-08	7.03E-08	10.5 %	0.00041 %	
Peru	TC221112(1)C	3.31	2.03	3.75	1.96E+10	10.27	0.03	292.51	1.05E-05	5.17E-06	8.20E-06	7.9 %	0.00009 %	−6.8
Peru	MI221116C	5.23	12.67	5.32	1.39E+10	10.47	0.03	292.15	3.87E-05	3.05E-06	1.73E-06	2.2 %	0.00002 %	−4.9
Peru	LL221118C	3.77	170.32	3.77	1.47E+10	9.86	0.03	302.55	1.09E-04	6.42E-07	1.69E-06	1.2 %	0.00002 %	−6.4
Peru	CA221118	3.64	2.11			9.98	0.03	291.84	4.76E-09	2.25E-09	1.43E-09	99.8 %		−7.4
Peru	KV221120	2.66	1.13			10.12	0.03	291.99	5.67E-06	5.00E-06	1.38E-05			
Peru	TG221122	0.66	35.67	0.65	5.20E+10	9.90	0.03	334.75	2.43E-07	6.82E-09	1.98E-08	89.5 %	0.00188 %	−6.9
Argentina	BF230316	0.80	0.41	0.13		9.65	0.0289	298.0	6.68E-07	1.62E-06	3.37E-06			
Argentina	CZ230307	1.89	138.47	1.90		9.82	0.0291	308.2	7.94E-04	5.73E-06	3.51E-05			−16.0
Argentina	ES230304	0.32	11,323.93	0.32	1.73E+07	9.89	0.0348	351.6	1.03E-03	9.13E-08	2.54E-06	11.2 %	1.44207 %	−12.2
Argentina	JB230315	0.45	55.17	0.45		9.79	0.0286	301.5	6.88E-05	1.25E-06	5.66E-06			
Argentina	LB230315	0.34	2886.76	0.34		9.69	0.0281	348.0	1.42E-03	4.93E-07	1.23E-05			
Argentina	LF230308	1.05	492.39	1.05	6.43E+08	9.88	0.0285	305.3	4.92E-05	1.00E-07	9.85E-07	31.8 %	0.03372 %	−8.6
Argentina	LN230313													
Argentina	LV230307	2.71	243.75	2.71		9.70	0.0286	305.5	1.82E-05	7.46E-08	9.31E-07			
Argentina	LV230309											86.2 %	0.04314 %	−11.1
Argentina	OY230308													
Argentina	OZ230305	1.03	66.82	1.03		10.01	0.0290	301.6	3.54E-05	5.29E-07	2.40E-06			
Argentina	PG230225													
Argentina	PI230308	1.32	2560.73	1.32	2.73E+08	9.38	0.0283	492.5	1.37E-05	5.34E-09	5.41E-08	18.5 %	0.03690 %	−11.9
Argentina	PQ230306	1.58	37.27	1.59	1.81E+07	9.68	0.0290	306.2	3.18E-04	8.54E-06	3.25E-05	0.8 %	0.01982 %	−13.4
Argentina	QH230313													
Argentina	RC1230306	2.77	17.31	2.80		10.01	0.0293	292.0	8.44E-08	4.87E-09	3.83E-08	99.1 %		−10.7
Argentina	TZ230310	5.19	30.46	5.23	2.76E+10	10.03	0.0302	295.5	1.55E-06	5.10E-08	4.59E-07	99.1 %	0.00050 %	−6.8
Argentina	VA230311													

Table 3
Noble gas isotope and carbon isotope data for water phase samples. Uncertainties are less than 5 % for all isotopes, concentrations, and elemental ratio reported. Noble gas data were acquired by static mass spectrometer in the Barry Lab at WHOI. Carbon (13C) measurements were done at OVSICORI. Radiocarbon (14C) measurements were made at NOSAMS at WHOI.

Region	Site ID	$^{3}He/^{4}He$	$^{4}He/^{20}Ne$	$^{3}He/^{4}He$	$CO_2/^{3}He$	$^{20}Ne/^{22}Ne$	$^{21}Ne/^{22}Ne$	$^{40}Ar/^{36}Ar$	^{4}He	^{20}Ne	^{36}Ar	DIC	$\delta^{13}C$ DIC	^{14}C DIC	^{14}C DIC	^{14}C DIC	^{14}C DIC
		R/R_A		R_C/R_A					$cm^3STP/g\ H_2O$	$cm^3STP/g\ H_2O$	$cm^3STP/g\ H_2O$	mol/l	vs PDB	F Modern	Fm Err	Age	Age Err
Chile	LC220316	1.06	0.27	2.10	3.49E+11				5.39E-08	2.00E-07		0.0012	−7.88	0.5325	0.0065	5060	100
Chile	QN220317	1.79	0.28	9.81	6.72E+11				2.82E-08	1.01E-07		0.0021	−8.63	0.8424	0.0092	1380	90
Chile	LN220321	1.57	12.49	1.58	#######				7.18E-07	5.75E-08		0.0013	−5.05	0.0330	0.0067	27,400	1600
Chile	GB220322	1.55	0.83	1.81	1.98E+12				1.93E-08	2.32E-08		0.0037	−3.53	0.0011	0.0059	> 39,800	43,500
Chile	CA220323	1.25	0.31	2.30	4.18E+11				3.46E-08	1.10E-07		0.0011	−1.5	0.1795	0.0059	13,800	270
Chile	CC220324	1.18	0.22	0.02	3.21E+11				2.64E-08	1.23E-07		0.0006		0.3661	0.0093	8070	200
Chile	CR220324	1.20	0.45	1.47	3.34E+11				3.05E-08	6.81E-08		0.0008		0.3658	0.0072	8080	160
Chile	OA220325	1.10	0.63	1.18	#######				9.38E-08	1.50E-07		0.0017		0.0623	0.0059	22,300	760
Chile	VA220325	1.04	1.19	1.05	2.15E+11				1.09E-07	9.14E-08		0.0015	0.49	0.0631	0.0059	22,200	750
Chile	TM220326	0.08	23.34	0.06	#######				2.63E-06	1.13E-07		0.0003	−10.88				
Chile	IS220328	2.01	0.41	3.70					3.07E-08	7.55E-08		0.0000		0.0005	0.0061	> 40,400	#######
Chile	PZ220330	1.74	6.03	1.77	6.32E+11				3.07E-08	5.08E-09		0.0021	−0.92	−0.0120	0.0060	> 41,100	
Chile	PJ220330	2.26	0.43	4.35	1.66E+11				6.60E-08	1.53E-07		0.0015	−5.46	0.0615	0.0060	22,400	780
Chile	EQ220330	2.84	3.21	3.01	1.68E+11				2.95E-07	9.20E-08		0.0087	−1.45	0.0049	0.0059	> 36,400	9800
Chile	TT220331	3.51	1.63	4.00	5.76E+11				4.61E-08	2.83E-08		0.0058					
Chile	LA220331											0.0048	3.93	−0.0064	0.0060	> 41,200	
Chile	LP220401	1.44	0.25		1.53E+11				4.03E-08	1.62E-07		0.0005	−5.21	0.6381	0.0160	3610	200
Chile	CP220402	1.91	1.42	2.12	2.16E+12				3.69E-07	2.59E-07		0.0941					
Chile	CE220402	2.55	1.19	2.98	6.18E+13				1.83E-09	1.53E-09		0.0179	0.58				
Chile	JR220403	0.92	17.93	0.92	1.48E+10				1.12E-06	6.25E-08		0.0009	−4.78	0.0104	0.0061	36,700	4700
Argentina	BF230316	0.88	0.31		2.86E+11	9.75	0.027	296.7	9.01E-08	2.89E-07	1.19E-06	0.0014	−8.26				
Argentina	CM230315	0.54	29.69		9.82E+09	7.44	0.0289	299.0	3.02E-06	1.02E-07	8.22E-07	0.0010	−8.55				
Argentina	CZ230307	1.90	54.70		1.15E+10	9.92	0.0333	296.0	2.45E-06	4.49E-08	3.96E-07	0.0033	−6.69				
Argentina	LF230308	1.14	21.96		1.16E+12			292.6	1.82E-07	8.27E-09	2.55E-08	0.0149	−6.49				
Argentina	LN230313	0.58	1049.79		1.20E+10			304.1	3.03E-05	2.88E-08	1.97E-07	0.0131	0.16	0.0166	0.0032	32,900	1500
Argentina	OY230308	0.74	19.39		3.84E+10	9.91	0.0286	297.0	1.51E-06	7.79E-08	6.48E-07	0.0026	−9.67				
Argentina	OZ230305	1.06	23.94		3.89E+11	9.71	0.0307	299.0	4.36E-07	1.82E-08	1.68E-07	0.0112	−6.19				
Argentina	PG230225	1.34	107.70	1.34					2.70E-06								
Argentina	PI230308	1.30	1.26		1.88E+13			291.3	3.07E-08	2.44E-08	2.52E-08	0.0464	−3.41				
Argentina	PQ230306											0.0055	−10.95	0.0424	0.0033	25,400	620
Argentina	QH230313	1.06	98.59		1.22E+09	8.04	0.0281	299.9	9.41E-06	9.54E-08	5.42E-07	0.0008	−8.9				
Argentina	RC1230306											0.0152	−4.15	0.0014	0.0038	> 42,200	22,000
Argentina	TZ230310											0.0102	−2.87	0.0296	0.0032	28,300	870
Argentina	VA230311	2.79	2.36		2.42E+12	9.67	0.0286	296.2	3.09E-07	1.31E-07	8.81E-07	0.1293	0.83				

Table 4
High precision dynamic mass spectrometry (DMS) data for the Pirquitas sample. Individual uncertainties are provided for each isotope ratio. DMS data were obtained in the Seltzer Lab at WHOI.

	$^{40}Ar/^{36}Ar$	error	$\delta^{38}Ar/^{36}Ar$	error	$\delta^{86}Kr/^{84}Kr$	error	$\delta^{86}Kr/^{82}Kr$	error	$\delta^{136}Xe/^{130}Xe$	error	$\delta^{134}Xe/^{130}Xe$	error	$\delta^{132}Xe/^{130}Xe$	error	$\delta^{131}Xe/^{130}Xe$	error	$\delta^{129}Xe/^{130}Xe$	error	$\delta^{128}Xe/^{130}Xe$	error
Pirquitas; PI230308	463.27	0.03	2.7	0.1	0.714	0.028	0.773	0.033	2.801	0.139	1.983	0.13	0.425	0.109	0.051	0.127	0.718	0.109	0.314	0.234

Table 5
Nitrogen isotope and clumped nitrogen isotope data for the Pirquitas sample. Individual uncertainties are provided for each isotope ratio. Data were measured in the Young Lab at UCLA.

	$\delta^{15}N$	±1s	$\Delta_{30}N$	±1s
Pirquitas; PI230308	+6.13	0.01	+0.79	0.30
Nitrogen isotopes in permil deviations from atmosphere				

rock (e.g., Hilton et al., 1993; Inostroza et al., 2020). We note that the residence time of these fluids in the crust is also likely much longer compared with high temperature volcanic gas emissions (e.g., summit fumaroles), as thermal springs require specific structural conditions (i.e., deep fault structures) and circuitous paths to reach the surface, whereas volcanic conduits likely allow a faster and more direct pathway for fluids to the surface. For these reasons, high temperature magmatic gases and olivine-hosted fluid inclusions from the CVZ indicate much higher mantle He percentages (de Moor et al., In Review). For example, our highest temperature gas sample (408 °C; 5.8 R_A), from Irruputuncu volcano, contains 72 % mantle He, and gas samples from Lascar volcano (Tassi et al., 2011) have $^3He/^4He$ values as high as 7.3 R_A, indicating 90 % mantle helium.

3.3.2. Carbon

Carbon in thermal spring samples can be derived from the mantle, the overlying crust, or from subducted carbon-rich sediments, which release volatiles that migrate to surface springs across the arc (e.g., Sano and Marty, 1995). $CO_2/^3He$ and $\delta^{13}C$ data have been extensively used to differentiate between various carbon sources; however, it is often challenging to distinguish between carbon additions from subduction versus those derived from the overlying crust.

Previous studies in the ACM have noted the role of subducted sediment-derived fluids in melting the Sub-Andean mantle (e.g., Stern, 2007) and supplying volatiles to hydrothermal fluid samples (Ray et al., 2009). Previous work from our group (i.e., Barry et al., 2022) indicated that He and C are likely released across the entire convergent margin (outer forearc, forearc, arc, backarc) and that adopting such a narrow view of where these volatiles are released is likely an oversimplification. It is therefore important to sample across the entire arc system, so that carbon output estimates can be more accurately compared with input estimates.

To quantify the extent of slab-derived CO_2 to thermal springs, we adopt the approach of Sano and Marty (1995), which uses observed He-CO_2 characteristics to deconvolute mantle- versus subduction-derived (i.e., organic sediments and inorganic limestones) components. This approach implicitly assumes that all $CO_2/^3He$ and $\delta^{13}C$ variations are the result of mixing between subduction and mantle derived components and that there is no crustal input from the overriding slab. We note that these assumptions may not be valid, and we explore alternative scenarios below. However, if these assumptions are in fact valid, He–CO_2 characteristics (relative abundances and $\delta^{13}C$ systematics) can be used to resolve CO_2 contributions from three distinct sources: limestone (L) from subducted sediment and mineralized within slab basement, sedimentary (organic) carbon (S) from subducted sediment, and the mantle wedge (M). Each endmember source component is assumed to have a distinctive $CO_2/^3He$ ($M = 2 \times 10^9$; $L = 1 \times 10^{13}$; $S = 1 \times 10^{13}$) and $\delta^{13}C$ ($M = -5‰$; $L = 0‰$; $S = -30‰$) signature. Notably, a recent study suggests that subducting sediments may be higher (~−22.5‰; Xu et al., 2021), which would change the relative contributions slightly. In Fig. 3, we plot the $CO_2/^3He$ values as a function of $\delta^{13}C$ for all samples, together with binary mixing trajectories. In order to quantify the relative proportions of CO_2 derived from each respective endmember component, mass fractions of three major sources of carbon are calculated following the methods of (Sano and Marty, 1995).

Using this approach, we calculate that the average CO_2 provenance in the CVZ to be L:S:M = 75:17:8, which is broadly similar to what Barry

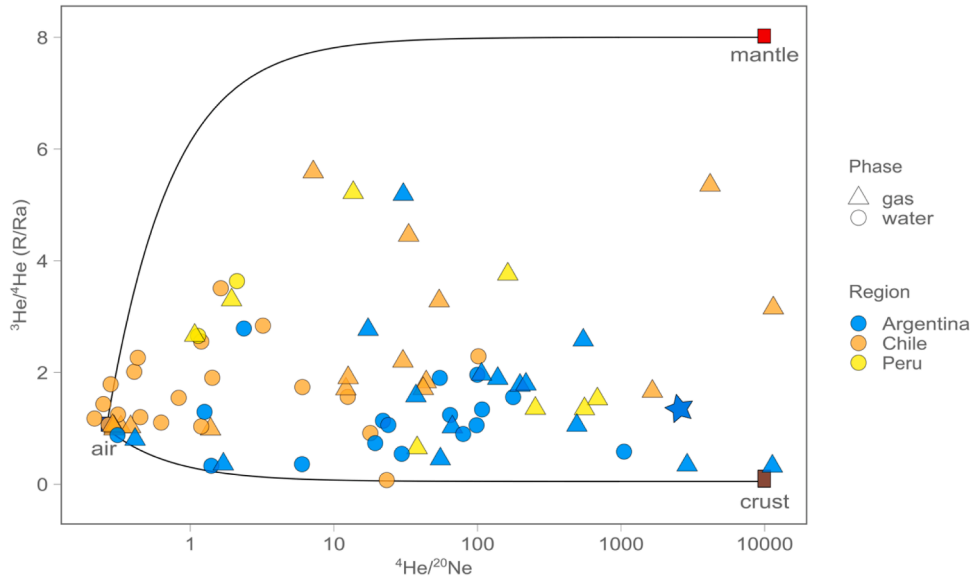

Fig. 2. Helium isotopes ($^3He/^4He$) vs. $^4He/^{20}Ne$ for gas (triangles) and water (circles) phase samples. Nearly all samples can be explained by three-component mixing between air, mantle (red square) and crust (brown square). As in all figures, the star symbol is used to denote gas phase sample PI230308 from Piquiras.

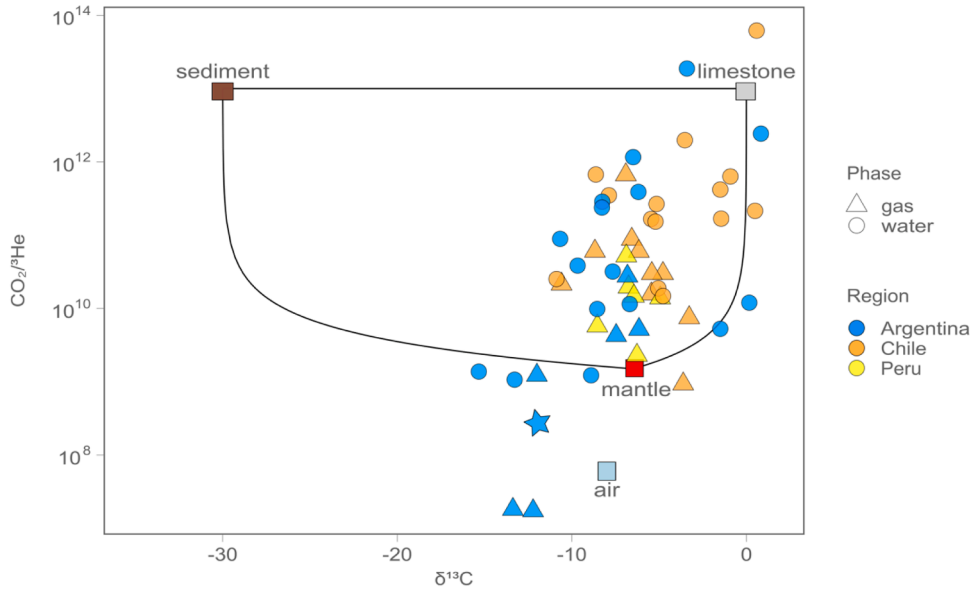

Fig. 3. $CO_2/^3He$ vs. $\delta^{13}C$ (‰) vs. PDVB of CO_2 for all gas (triangles) and DIC for water (circles) samples respectively from this study. The uncertainties on the $CO_2/^3He$ vs. $\delta^{13}C$ of CO_2 data are lower than given by the size of the symbols. Subduction-related source end-member compositions for mantle (M), limestone (L), and sediment (S) are plotted for reference, along with binary mixing lines between these three endmember, after Sano and Marty (1995). For reference, air is also plotted. Notably, calcite deposition or dissolution processes could result in the values that plot below the mixing envelope. As in all figures, the star symbol is used to denote gas phase sample PI230308 from Piquiras.

et al. (2022) found (L:S:M = 70:22:8) using an entirely separate set of samples from the CVZ. These calculations equate to an average L/S of 4.9 (this work) versus an average L/S 3.2 in Barry et al. (2022) and an average ($L + S$)/M of 11.9 for the CVZ, which is identical to what Barry et al. (2022) found. This approach implies that slab-derived contributions dominate the CO_2 budget. See Barry et al. (2022) for a more detailed discussion about this approach and its limitations.

The above approach assumes all He-C characteristics are controlled by subduction and mantle inputs and that there is no significant input of assimilated crustal CO_2. While this assumption is likely valid for high temperature volcanic arc samples (e.g., fumaroles) marked by high $^3He/^4He$, here we report thermal spring data from across the entire arc system (i.e., forearc, arc, backarc), with a wide range in $^3He/^4He$. An alternative explanation is that crustal assimilation may be modifying $CO_2/^3He$ and $\delta^{13}C$. This hypothesis is compelling in the CVZ, due to the exceedingly thick crust and evidence of carbonate assimilation in some CVZ melts (Matthews et al., 1996). However, $\delta^{13}C$ values that are lower than typical mantle and carbonate values (Fig. 3) suggests either incorporation of isotopically light organic carbon in the crust, perhaps from sediments (Sano and Marty, 1995; DeCelles et al., 2011; Quade et al., 2015; Giambiagi et al., 2022), or a negative carbon isotope excursion due to carbonate precipitation (Fig. 3) at depth (Ray et al., 2009; Barry et al., 2019; 2022). Notably, the crustal assimilation hypothesis is supported by He isotope data (Barry et al., 2022), which are highly variable and lower on average versus typical arcs (Hilton et al., 2002), suggesting significant radiogenic overprinting due to interaction

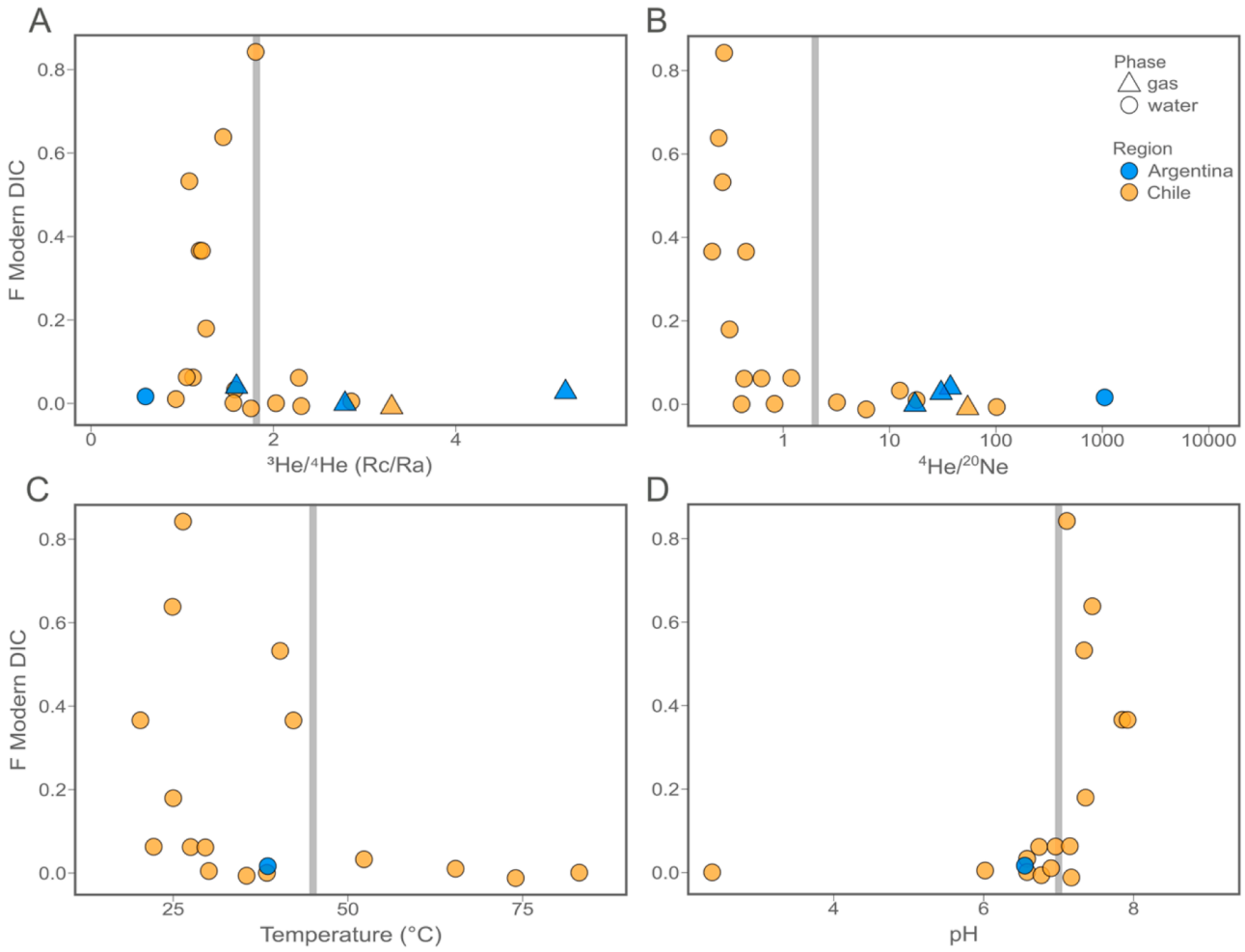

Fig. 4. a-d. Radiocarbon (^{14}C) activities (expressed as fraction modern dissolved inorganic carbon (F^{14}C DIC) vs ^{3}He/^{4}He (Fig. 4a), ^{4}He/^{20}Ne (Fig. 4b), Temperature (Fig. 4c) and pH (Fig. 4d). The gray vertical lines illustrate the bimodal nature of the data. Notably, a handful (n = 4) gas samples are plotted on Figs. 4a and 4b, where there are water phase ^{14}C data, but no corresponding water phase He-Ne data, in which case we plot the gas phase ^{3}He/^{4}He and ^{4}He/^{20}Ne from that particular site against F modern DIC.

with the crust. In Section 3.3.1 we suggested that He isotope variations are primarily controlled by the thickness of the crust, with approximately 77 % of helium derived from the crust on average in thermal springs from this study. We surmise that similar processes could affect the carbon systematics, as $CO_2/^3He$ is higher (1.6×10^{12}) than the mantle on average in the CVZ (1-sigma standard deviation = 8.3×10^{12}). Additionally, $\delta^{13}C$ is −7.9‰ (1-sigma standard deviation = 3.5‰) is lighter than the mantle on average in the CVZ. Notably, if only arc samples are considered (de Moor et al., In Review), the average $CO_2/^3He$ is significantly lower and $\delta^{13}C$ is isotopically higher than mantle, meaning these lower temperature thermal spring samples heavily skew the average $\delta^{13}C$ to lighter values.

Carbon removal due to calcite precipitation or gas dissolution is yet another process that can affect $CO_2/^3He$ and $\delta^{13}C$. However, there is not strong evidence for carbon loss in Chile samples and most data fall within the mixing envelope in Fig. 3. Peru thermal spring data span a much wider range, with $CO_2/^3He$ spanning ~7 orders of magnitude. Argentina has two data points clearly below the mantle line, and interestingly these have the lowest $\delta^{13}C$ values observed, suggesting that calcite precipitation may be occurring in this region (e.g., Ray et al., 2009; Barry et al., 2022). Similarly, gas loss due to dissolution in water can also result in a decrease in $CO_2/^3He$ in both gas and water phase samples (Gilfillan et al., 2009; Güleç and Hilton, 2016). Notably, the trends that are predicted are similar to those anticipated from calcite precipitation (e.g., Güleç and Hilton, 2016). In short, as gases ascend towards the surface, they likely come into contact with gas-undersaturated aquifers. When this occurs, the gas phase preferentially loses the more soluble gas species (i.e., C) relative to the less soluble gas species (i.e., He), resulting in lower $CO_2/^3He$ in the gas phase which ultimately manifests at the surface (Barry et al., 2022).

3.4. Neon and argon isotopes

Neon and argon isotopes are not routinely reported in thermal spring samples, as they are commonly air-dominated. In CVZ thermal spring samples, most Ne isotope data (Tables 2 and 3) indeed cluster around air values, which is consistent with our understanding of the overall mass balance of volatiles in volcanic hydrothermal systems, whereby small amounts of atmospheric Ne circulating in the hydrothermal system can easily overwhelm the deep (crustal and mantle) signals. For this reason, Ne isotopes are of somewhat limited utility for interpreting source features in thermal spring samples. Argon isotopes in isolation cannot distinguish between crustal and mantle sources, as both are marked by elevated ^{40}Ar/^{36}Ar values relative to air. Instead, Ar isotope data are best interpreted alongside other tracers (e.g., He, C, Xe, N_2 isotopes). In CVZ thermal spring samples, Ar isotopes vary from 296 to 492 (for reference, air ^{40}Ar/^{36}Ar = 298.6) and point toward mixing between a crustal endmember, marked by radiogenic ^{3}He/^{4}He and non-atmospheric ^{40}Ar/^{36}Ar and a second endmember with variable ^{3}He/^{4}He (i.e., between air and mantle) and broadly air-like ^{40}Ar/^{36}Ar

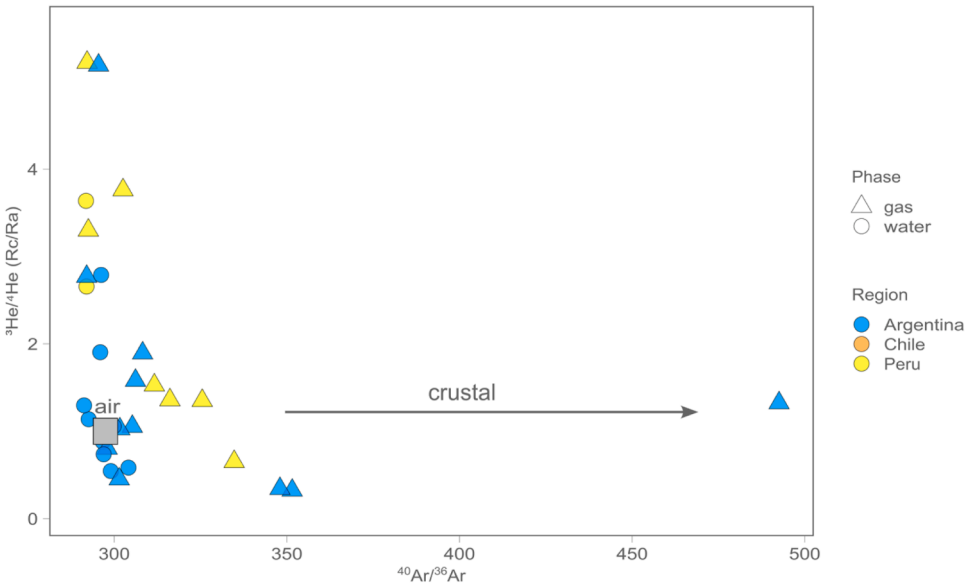

Fig. 5. He isotopes vs Ar isotopes. Ar isotopes vary from 296 to 492 (for reference, air $^{40}Ar/^{36}Ar = 298.6$) and point towards mixing between a crustal endmember, marked by radiogenic $^{3}He/^{4}He$ and non-atmospheric $^{40}Ar/^{36}Ar$ and a second endmember with variable $^{3}He/^{4}He$ (i.e., between air and mantle) and broadly air-like $^{40}Ar/^{36}Ar$. Uncertainties on He isotopes are better than 5 %, and uncertainties on Ar isotopes are better than 6 %.

(Fig. 5). Again, mass balance considerations can explain this trend, whereby mantle He isotope anomalies are observed in several samples, even when Ar isotopes are swamped by atmospheric contributions, suggesting decoupling between He and Ar.

3.5. *High precision Ar, Kr and Xe*

High precision Ar, Kr, and Xe results are reported in Table 4. Data were obtained using dynamic mass spectrometry (DMS), which yields significantly higher analytical precision relative to traditional static (SMS) noble gas techniques (methods described in Seltzer and Bekaert, 2022). High precision DMS $^{40}Ar/^{36}Ar$ values for the Pirquitas sample

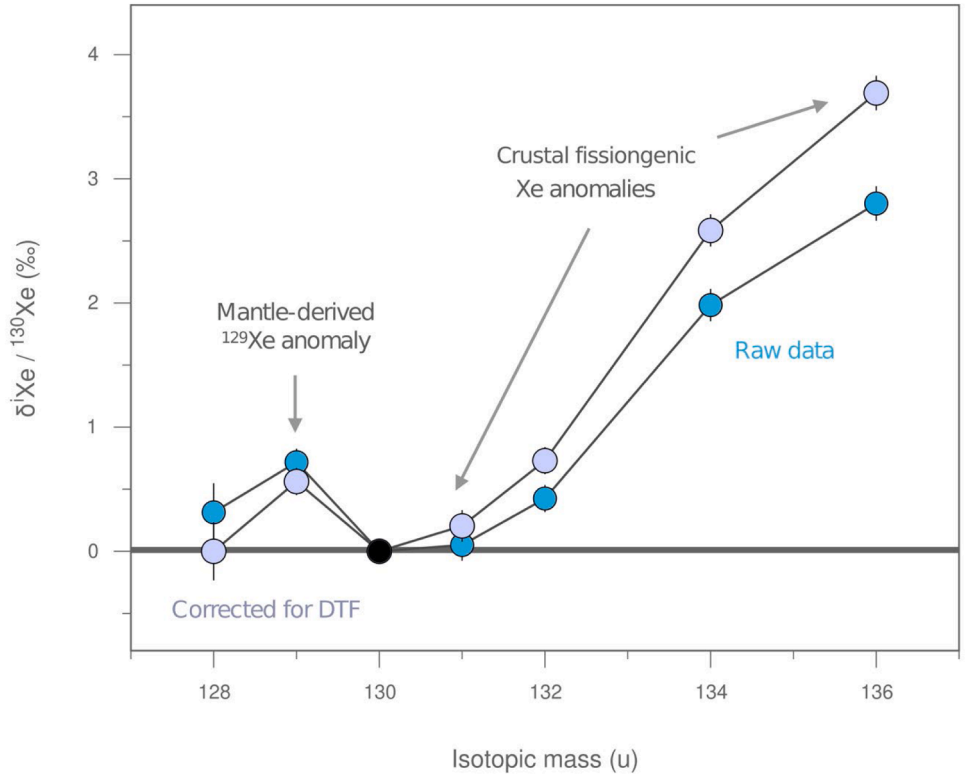

Fig. 6. Xenon spectra for the Pirquitas sample. Assuming a pure mantle $^{129}Xe^{*}/^{136}Xe^{*} \sim 1$, then the observed $^{136}Xe/^{129}Xe$ of 3.9 suggests that only 12 % of the $^{136}Xe^{*}$ is coming from the mantle, with the reminder (88 %) deriving from the crust. This agrees remarkably well with He isotope constraints, which independently implies a 84 % mantle contribution to the Pirquitas sample.

($^{40}Ar/^{36}Ar = 463.27 \pm 0.03$) are in broad agreement with SMS results from the Barry Lab ($^{40}Ar/^{36}Ar = 492 \pm 30$), with both values being in marked excess of the atmospheric ratio ($^{40}Ar/^{36}Ar = 296.8$; Lee et al. 2006). While most $^{40}Ar/^{36}Ar$ values measured in subduction zones worldwide exhibit only slight - if any - excesses relative to the atmospheric value (Bekaert et al., 2023), the elevated $^{40}Ar/^{36}Ar$ observed in the Pirquitas sample (Fig. 5) reflects the contribution of radiogenic ^{40}Ar ($^{40}Ar^*$) from radioactive decay of ^{40}K via electron capture in the continental crust and/or mantle.

One way to distinguish between crustal and mantle-derived noble gas inputs is to use Xe isotope systematics (Fig. 6). This is because the mantle exhibits a marked excess of ^{129}Xe ($^{129}Xe^*$) relative to primordial Xe isotopes (e.g., ^{130}Xe) when normalized to the atmospheric composition, due to the radiogenic decay of ^{129}I ($T_{1/2} = 15.7$ Myr) within the first ~100 Myr of our planet's evolution. Here, we observe that the high precision Xe isotope composition of Pirquitas indeed exhibits a significant $^{129}Xe^*$, which is however accompanied by additional excesses in the light (^{128}Xe) and heavy ($^{131-136}Xe$) isotopes. The latter reflects the contribution of fissiogenic Xe production via spontaneous fission of now extinct ^{244}Pu ($T_{1/2} = 80$ Myr) and/or still extant ^{238}U ($T_{1/2} = 4.468$ Gyr) (Porcelli and Ballentine 2002). While the mantle still preserves some minor remnants of fissiogenic Xe from ^{244}Pu (Kunz et al., 1998; Bekaert et al., 2024), crustal environments are characterized by pure ^{238}U-derived Xe excesses. Thus, both the mantle and crust may contribute heavy, fissiogenic Xe isotopes to the Pirquitas gas sample. Regarding the ^{128}Xe excess, there are two potential explanations, neither of which involve nuclear reactions. The first one is the occurrence of a deep, primordial component that is mass dependently enriched in the light Xe isotopes relative to the present-day atmosphere (as would for instance be expected if the Earth had preserved a chondritic Xe isotope component, inherited from its planetary building blocks; e.g., Caffee et al., 1999; Holland and Ballentine, 2006; Broadley et al., 2020). The second possibility is physical fractionation of the noble gas signals within hydrothermal systems, via diffusive transport fractionation (DTF; Bekaert et al., 2023). In both cases, propagating the correction for the occurrence of this mass dependent light Xe isotope enrichment toward heavier isotopes would tend to exacerbate the heavy Xe isotope excesses observed from the raw data.

Here, we rely on both (i) the recent finding that the upper mantle is largely devoid of primordial heavy noble gases (Bekaert et al., 2024), and (ii) the fact that non-radiogenic Kr and Xe isotope systematics for the Pirquitas sample are consistent with the global diffusive transport fractionation (DTF) line (Fig. 7), to correct for physical fractionation of Xe isotopes in the Pirquitas gas using Kr isotope systematics (Fig. 7; Bekaert et al. 2023). We find that the heavy fissiogenic Xe isotope excesses are much greater than expected based on the $^{129}Xe^*$ (typical $^{129}Xe^*/^{136}Xe^* \sim 1$ for most mantle sources worldwide; Bekaert et al. 2024; Marty et al., in review), indicating significant contribution from crustal (^{238}U-derived) Xe. Assuming a pure mantle $^{129}Xe^*/^{136}Xe^* \sim 1$ (Bekaert et al., 2019, 2024; Marty et al., in review), then the observed $^{136}Xe/^{129}Xe$ of 3.9 suggests that only 12 % of the $^{136}Xe^*$ is coming from the mantle, with the remainder (88 %) deriving from the crust. This agrees remarkably well with He isotope constraints, which independently implies a 84 % crustal contribution to the Pirquitas sample. To our knowledge this is the first time that both He and Xe isotopes have yielded such close agreement in a subduction related sample. This result also appears consistent with the large amount of $^{40}Ar^*$, with both signatures arguably arising from the occurrence of an anomalously thick

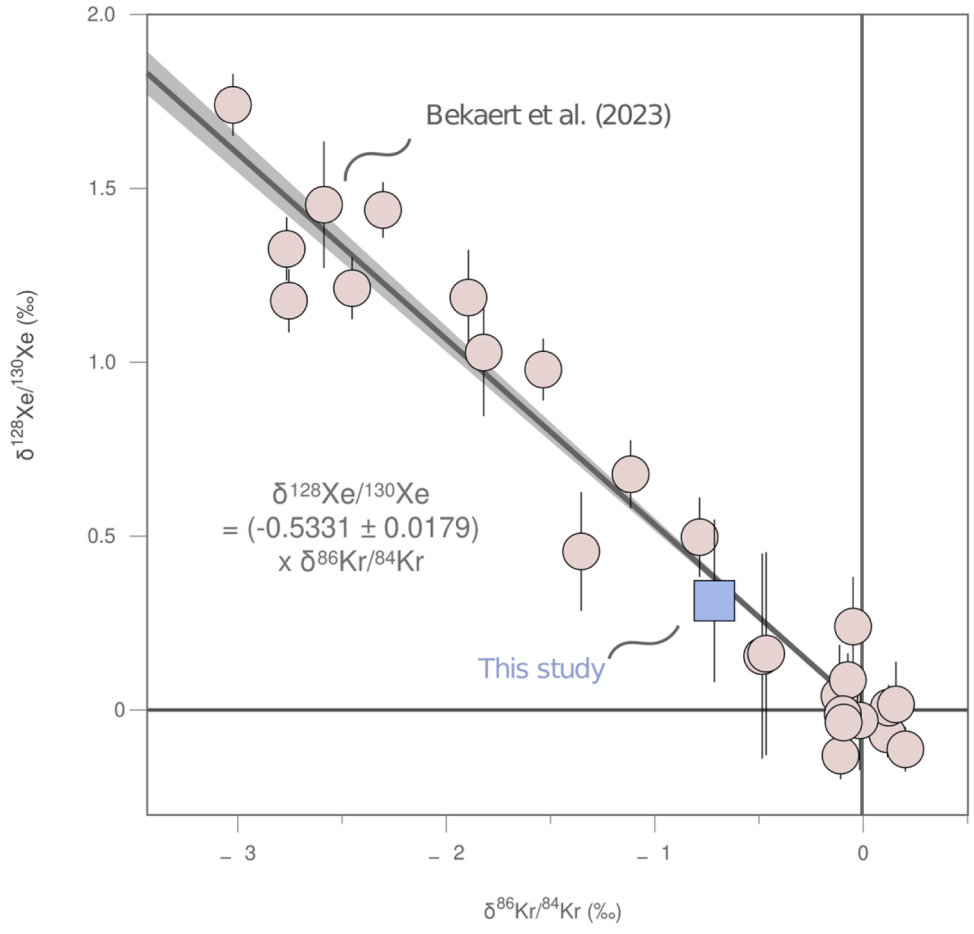

Fig. 7. Xe isotopes vs Kr isotopes from various hydrothermal spring samples. All data are from Bekaert et al., 2023, apart from the Pirquitas sample (this study), which plots along the global diffusive transport fractionation (DTF) line. As such, a correction can be applied to all Xe isotope data to account for DTF.

continental crust in this part of the CVZ. Xenon isotopes were not measured in other samples, due to low $^{40}Ar/^{36}Ar$, implying that Xe isotopes will essentially be indistinguishable from air (Bekaert et al., 2023).

3.6. Clumped N_2

We also measured clumped N_2 isotopes ($^{15}N^{15}N$) (Young et al., 2016; Yeung et al., 2017; Labidi et al., 2020; 2021) in the Pirquitas sample (Table 5). Specifically, we use $^{15}N^{15}N$ to estimate the extent of sample contamination by atmospheric nitrogen, the most abundant gas in air. We use the Δ_{30} notation, whereby the $^{15}N^{15}N$ concentration is reported relative to a random distribution of ^{14}N and ^{15}N atoms among N_2 molecules, as expected for equilibrium at high temperature. The Δ_{30} tracer is defined as $\Delta_{30}={}^{30}R/({}^{15}R)^2 - 1$ (‰), where $^{30}R= {}^{15}N^{15}N/ {}^{14}N^{14}N$ and $^{15}R={}^{15}N/{}^{14}N$. N_2 formed by geological processes at high temperatures (i.e., ~800 °C; Yeung et al., 2017), results in equilibrium among N_2 isotopologues reflected by Δ_{30} values from 0.5 to 0.1‰, respectively (Yeung et al., 2017). This applies for all deeply-derived (i.e., magmatic and crustal) N_2, (Labidi et al., 2020). In contrast, air has a diagnostic disequilibrium $^{15}N^{15}N$ enrichment, resulting in an atmospheric Δ_{30} value of 19.1 ± 0.3‰ (2σ) (Yeung et al., 2017), although high temperatures (>800 °C) may also reorder atmospheric N_2 towards high temperature equilibrium (Yeung et al., 2017).

We find a Δ_{30} of 0.79 ± 0.30‰ and a $\delta^{15}N$ of +6.13 ± 0.01‰ for the Pirquitas sample. In Fig. 8, we plot the Pirquitas sample together with eight fumaroles and seven bubbling springs from a previous study (Labidi et al., 2021) of arc gases from Central America. In light of the high N_2/Ar (=1445) of this sample (>17 times greater than the atmospheric N_2/Ar ratio), it is clear that geologically-sourced N_2 must dominate the N_2 content in this system. The finding of Δ_{30} ~ 0‰ confirms that any atmospheric N_2 content is negligible relative to the large geogenic component (Fig. 8). The fact that He and Xe isotopes both indicate that the Pirquitas sample is composed of >84 % crustal and <16 % mantle gas suggests that the positive $^{15}N^{15}N$ in Pirquitas also likely reflects a predominantly crustal signal. We surmise that this low Δ_{30} nitrogen component, marked by a crustal-like $\delta^{15}N$ value, reflects formation of N_2 at high temperature in the crust, while preserving the original $\delta^{15}N$. This would imply that the thick crust beneath the CVZ is effectively being baked and co-releasing N_2 and noble gases (He through Xe) to the surface. We surmise that He and Xe are coupled and effectively released from the crust due to interaction with the Altiplano-Puna Magma Body (APMB) (Fig. 1), beneath the Pirquitas region. Alternatively, the N_2 signature could be a direct result of sufficiently heated subducted N in sediments, resulting in low Δ_{30}, but decoupled from noble gases and C systematics. The first scenario is more plausible, as it does not require decoupling between different volatile elements. However, differentiating between old overlying crust-derived and subduction (N_2-rich) related fluids is difficult. Notably, the APMB (the largest magma body on Earth) is located directly below the CVZ and provides a potential mechanism for the high temperature release of crustal volatiles (i.e., He, Ar, Xe and N_2) towards the surface. Notably, ignimbrites in the CVZ are sourced by crustal derived magmas (i.e., APMB), whereby intruding magmas resulted in crustal melting and assimilation. This led to the development of crustal-scale intrusive complexes and eventually the APVC (de Silva et al., 2006) in the CVZ. Our combined noble gas and clumped N_2 results indicate these crustally-influenced magmas are the source of the volatiles in the thermal springs throughout the region as well.

4. Summary

When taken together, carbon, noble gases and clumped N_2 isotopes data from thermal springs in the CVZ point towards a dominantly crustal source of volatile elements. The salient take-home points are:

- He-C isotope data are remarkably consistent with previous studies from the CVZ and suggest volatiles released by thermal springs in the CVZ are dominantly sourced from the crust (~77 %), with smaller (~23 %) mantle contributions.
- He-C isotopes are still the "gold-standard" for tracing source features in thermal springs, due to mass balance constraints.
- Thermal spring samples with non-atmospheric He-Ne characteristics have low radiocarbon activities, indicating that dissolved carbon (available for use by microbes) is deeply (i.e., mantle and crustal) derived and old (>22,000 years).

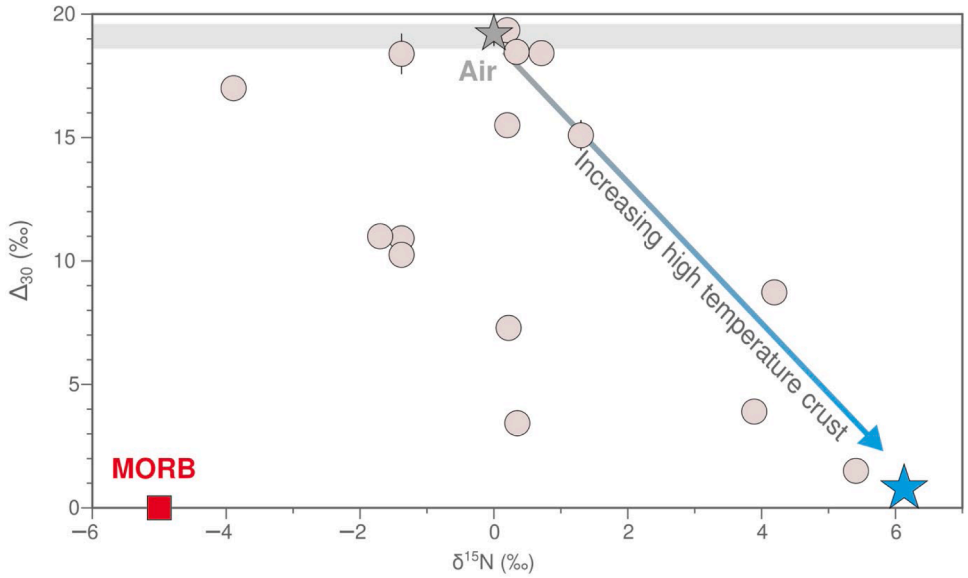

Fig. 8. The nitrogen isotopic composition of volcanic discharges in central America (gray circles) as reported by Labidi et al., 2021 together with the Pirquitas sample (this study; blue star). Variable Δ30 values indicated that Central America arc samples have variable amounts of atmospheric nitrogen. The Pirquitas sample (this study), has the lowest Δ30 value of all arc samples, implying the lowest air-derived N_2 contributions of any known arc sample. Similarly to the findings of Labidi et al., 2021, the high-temperature components (Δ30 approaching zero) have positive $\delta^{15}N$ values. The fact that He, C and Xe strongly suggest that this sample is >80 % crustal and <20 % mantle, suggests that we are observing high temperature crustal nitrogen.

- Argon isotope anomalies are most apparent in the Pirquitas gas sample from the Argentinian backarc.
- High precision Xe isotopes in the Pirquitas gas sample suggest a similar amount of crustal and mantle Xe as suggested independently by He isotopes. This points to a coupled release of all crustal noble gases, likely requiring bulk degassing of the crust via melting rather than low-temperature diffusive loss.
- Clumped N_2 results suggest that the Pirquitas gas sample has essentially no air-derived N_2 and suggests that crustal N_2 (and not just magmatic N_2) can be released at high temperatures (i.e., those marked by Δ_{30} of ~0‰).
- Future microbiological studies that aim to characterize the deep biosphere should target samples with 1) low (<0.1) ^{14}C activities, 2) non-atmospheric He isotopes (>1.8 R_A or <0.5 R_A), 3) elevated (>2) $^4He/^{20}Ne$, and 4) temperatures > 45 °C.

CRediT authorship contribution statement

PH Barry: Conceptualization, Funding acquisition, Investigation, Writing – original draft. **JM de Moor:** Writing – review & editing, Writing – original draft, Methodology, Formal analysis, Conceptualization. **MW Broadley:** Writing – review & editing, Writing – original draft, Formal analysis, Data curation. **AM Seltzer:** Writing – review & editing, Writing – original draft, Visualization, Methodology, Formal analysis, Data curation. **DV Bekaert:** Writing – review & editing, Writing – original draft, Visualization, Formal analysis, Data curation, Conceptualization. **K Patil:** Writing – review & editing, Formal analysis, Data curation. **CGE Bartels:** Writing – review & editing, Formal analysis, Data curation. **ED Young:** Writing – review & editing, Formal analysis, Data curation. **BE Longworth:** Writing – review & editing, Formal analysis. **B Barosa:** Writing – review & editing, Formal analysis. **A Bastianoni:** Formal analysis. **D Bastoni:** Formal analysis. **M Cascone:** Formal analysis. **SJ Turner:** Writing – review & editing, Writing – original draft, Formal analysis, Conceptualization. **RL Tyne:** Writing – review & editing, Writing – original draft, Formal analysis, Data curation. **M Anderson:** Writing – review & editing. **K Li:** Writing – review & editing. **J Curtice:** Formal analysis, Data curation. **N Kumar:** Writing – review & editing, Formal analysis. **GL Jessen:** Writing – review & editing, Writing – original draft, Funding acquisition. **JM Blamey:** Writing – review & editing, Conceptualization. **CJ Ramírez:** Writing – review & editing, Investigation, Conceptualization. **A Chiodi:** Writing – review & editing, Writing – original draft, Formal analysis, Data curation. **F Aguilera:** Writing – review & editing, Writing – original draft. **S Layana:** Writing – review & editing, Conceptualization. **C González:** Writing – review & editing. **M Aguilera:** Writing – review & editing, Conceptualization. **GPJ Masías Alvarez:** Investigation, Writing – review & editing. **B Marty:** Writing – review & editing, Conceptualization. **KG Lloyd:** Writing – review & editing, Writing – original draft, Supervision, Methodology, Investigation, Funding acquisition, Formal analysis, Data curation, Conceptualization. **D Giovannelli:** Writing – review & editing, Writing – original draft, Visualization, Supervision, Methodology, Investigation, Funding acquisition, Formal analysis, Data curation, Conceptualization.

Declaration of competing interest

Lead author Barry declares that none of the authors have any financial or personal relationships with other people or organizations that could inappropriately influence or bias this work.

Acknowledgments

This work was supported by NSF award 2121637 to PHB, JMdM, and KGL. We also acknowledge NSF awards 2152551 to PHB and KGL and 2151120 to PHB, AMS and DVB. DG has received funding from the European Research Council (ERC) under the European Union's Horizon 2020 research and innovation programme (grant agreement No 948972) acronym CoEvolve. GLJ acknowledges COPAS COASTAL ANID FB210021. MWB acknowledges support from NERC grant NE/X01732X/1. RLT acknowledged support from the Weston Howland Junior and Dame Kathleen Ollerenshaw Fellowships. FA, SL, CG and MA acknowledge the FONDECYT project (1211220) as well as the Millennium Scientific Initiative (ICN_038) and the Millennium Institute on Volcanic Risk Research - Ckelar Volcanes. Additionally, SL acknowledges a FONDECYT postdoctoral project (3240283). We acknowledge WHOI's NOSAMS facility, where ^{14}C measurements were made and Susan Lang and Roberta Hansman for consulting on these data. We thank the field participants in the 2022 Chile, 2023 Argentina and 2023 Peru field campaigns. We would also like to thank Lauren Tafla, Sarah Marcum and Jiarui Liu for their help in running clumped nitrogen isotopes at UCLA.

Supplementary materials

Supplementary material associated with this article can be found, in the online version, at doi:10.1016/j.epsl.2024.119169.

Data availability

Data will be made available on request.

References

Aguilera, F., Apaza, F., Del Carpio, J., Grosse, P., Jiménez, N., Ureta, G., Inostroza, M., Báez, W., Layana, S., Gonzalez, C., Rivera, M., 2022. Advances in scientific understanding of the Central Volcanic Zone of the Andes: a review of contributing factors. Bull. Volcanol. 84 (3), 22.

Barry, P.H., Hilton, D.R., Fischer, T.P., De Moor, J.M., Mangasini, F., Ramirez, C., 2013. Helium and carbon isotope systematics of cold "mazuku" CO2 vents and hydrothermal gases and fluids from Rungwe Volcanic Province, southern Tanzania. Chem. Geol. 339, 141–156.

Barry, P.H., De Moor, J.M., Giovannelli, D., Schrenk, M., Hummer, D.R., Lopez, T., Pratt, C.A., Segura, Y.A., Battaglia, A., Beaudry, P., Bini, G., 2019. Forearc carbon sink reduces long-term volatile recycling into the mantle. Nature 568 (7753), 487–492.

Barry, P.H., De Moor, J.M., Chiodi, A., Aguilera, F., Hudak, M.R., Bekaert, D.V., Turner, S.J., Curtice, J., Seltzer, A.M., Jessen, G.L., Osses, E., 2022. The helium and carbon isotope characteristics of the Andean Convergent Margin. Frontiers in Earth Science 10, 897267.

Basili, M., Rogers, T.J., Nakagawa, M., Yücel, M., de Moor, J.M., Barry, P.H., Schrenk, M. O., Jessen, G.L., Zahirovic, S., Bekaert, D. and Ramirez, C.J., 2024. Subsurface microbial community structure shifts along the geological features of the Central American Volcanic Arc.

Bekaert, D.V., Turner, S.J., Broadley, M.W., Barnes, J.D., Halldórsson, S.A., Labidi, J., Wade, J., Walowski, K.J., Barry, P.H., 2021. Subduction-driven volatile recycling: a global mass balance. Annu. Rev. Earth Planet. Sci. 49 (1), 37–70.

Bekaert, D.V., Barry, P.H., Broadley, M.W., Byrne, D.J., Marty, B., Ramírez, C.J., de Moor, J.M., Rodriguez, A., Hudak, M.R., Subhas, A.V., Halldórsson, S.A., 2023. Ultrahigh-precision noble gas isotope analyses reveal pervasive subsurface fractionation in hydrothermal systems. Sci. Adv. 9 (15), eadg2566.

Bekaert, D.V., Caracausi, A., Marty, B., Byrne, D.J., Broadley, M.W., Caro, G., Barry, P.H., Seltzer, A.M., 2024. The low primordial heavy noble gas and 244Pu-derived Xe contents of Earth's convecting mantle. Earth Planet. Sci. Lett. 642, 118886.

Broadley, M.W., Barry, P.H., Bekaert, D.V., Byrne, D.J., Caracausi, A., Ballentine, C.J., Marty, B., 2020. Identification of chondritic krypton and xenon in Yellowstone gases and the timing of terrestrial volatile accretion. Proceed. National Acad. Sci. 117 (25), 13997–14004.

Butler, W.A., Jeffery, P.M., Reynolds, J.H., Wasserburg, G.J., 1963. Isotopic variations in terrestrial xenon. J. Geophys. Res. 68 (10), 3283–3291.

Caffee, M.W., Hudson, G.B., Velsko, C., Huss, G.R., Alexander Jr, E.C., Chivas, A.R., 1999. Primordial noble gases from Earth's mantle: identification of a primitive volatile component. Science 285 (5436), 2115–2118.

Clift, P.D., 2017. A revised budget for Cenozoic sedimentary carbon subduction. Reviews of Geophysics 55 (1), 97–125.

DeCelles, P.G., Carrapa, B., Horton, B.K., Gehrels, G.E., 2011. Cenozoic foreland basin system in the central Andes of northwestern Argentina: implications for Andean geodynamics and modes of deformation. Tectonics 30 (6).

D'Hondt, S., Pockalny, R., Fulfer, V.M., Spivack, A.J., 2019. Subseafloor life and its biogeochemical impacts. Nat. Commun. 10 (1), 3519.

de Moor, J.M., Barry, P.H., Rodríguez, J., Aguilera, F., Aguilera, M., Gonzalez, C., Layana, S., Chiodi, A., Apaza, F., Masias, P., Kern, C., Barnes, J., Cullen, J., Bastoni, D., Bastianoni, A., Cascone, M., Jimenez, C., Salas-Navarro, J., Ramírez, C. J., Jessen, G., Giovannelli, D., Lloyd, K., 2024. Origins and Fluxes of Gas Emissions from the Central Volcanic Zone of the Andes. EPSL. In Review.

de Silva, S.L., Francis, P., 1991. Volcanoes of the Central Andes, 21. Springer-Verlag, Berlin, 6.
de Silva, S., Zandt, G., Trumbull, R., Viramonte, J.G., Salas, G., Jiménez, N., 2006. Large ignimbrite eruptions and volcano-tectonic depressions in the Central Andes: a thermomechanical perspective. In: Geological Society, London, Special Publications, 269, pp. 47–63.
de Silva, S.L., Kay, S.M., 2018. Turning up the heat: high-flux magmatism in the Central Andes. Elements: An Int. Magazine of Mineral., Geochem., Petrol. 14 (4), 245–250.
Fullerton, K.M., Schrenk, M.O., Yücel, M., Manini, E., Basili, M., Rogers, T.J., Fattorini, D., Di Carlo, M., d'Errico, G., Regoli, F., Nakagawa, M., 2021. Effect of tectonic processes on biosphere–geosphere feedbacks across a convergent margin. Nat. Geosci. 14 (5), 301–306.
Giambiagi, L., Tassara, A., Echaurren, A., Julve, J., Quiroga, R., Barrionuevo, M., Liu, S., Echeverría, I., Mardónez, D., Suriano, J., Mescua, J., 2022. Crustal anatomy and evolution of a subduction-related orogenic system: insights from the Southern Central Andes (22-35 S). Earth-Sci. Rev. 232, 104138.
Gilfillan, S.M., Lollar, B.S., Holland, G., Blagburn, D., Stevens, S., Schoell, M., Cassidy, M., Ding, Z., Zhou, Z., Lacrampe-Couloume, G., Ballentine, C.J., 2009. Solubility trapping in formation water as dominant CO2 sink in natural gas fields. Nature 458 (7238), 614–618.
Giovannelli, D., Barry, P.H., de Moor, J.M., Jessen, G.L., Schrenk, M.O., Lloyd, K.G., 2022. Sampling across large-scale geological gradients to study geosphere–biosphere interactions. Front. Microbiol. 13, 998133.
Giovannelli, D., 2023. Trace metal availability and the evolution of biogeochemistry. Nature Reviews Earth & Environment 4 (9), 597–598.
Güleç, N., Hilton, D.R., 2016. Turkish geothermal fields as natural analogues of CO2 storage sites: gas geochemistry and implications for CO2 trapping mechanisms. Geothermics 64, 96–110.
Hay Mele, B., Monticelli, M., Leone, S., Bastoni, D., Barosa, B., Cascone, M., Migliaccio, F., Montemagno, F., Ricciardelli, A., Tonietti, L., Rotundi, A., 2023. Oxidoreductases and metal cofactors in the functioning of the earth. Essays Biochem. 67 (4), 653–670.
Hilton, D.R., Hammerschmidt, K., Teufel, S., Friedrichsen, H., 1993. Helium isotope characteristics of Andean geothermal fluids and lavas. Earth Planet. Sci. Lett. 120 (3–4), 265–282.
Hilton, D.R., Fischer, T.P., Marty, B., 2002. Noble gases and volatile recycling at subduction zones. Rev. Mineral. Geochem. 47 (1), 319–370.
Hilton, D.R., 1996. The helium and carbon isotope systematics of a continental geothermal system: results from monitoring studies at Long Valley caldera (California, USA). Chem. Geol. 127 (4), 269–295.
Holland, G., Ballentine, C.J., 2006. Seawater subduction controls the heavy noble gas composition of the mantle. Nature 441 (7090), 186–191.
Inostroza, M., Tassi, F., Aguilera, F., Sepúlveda, J.P., Capecchiacci, F., Venturi, S., Capasso, G., 2020. Geochemistry of gas and water discharge from the magmatic-hydrothermal system of Guallatiri volcano, northern Chile. Bull. Volcanol. 82, 1–16.
Kallmeyer, J., Pockalny, R., Adhikari, R.R., Smith, D.C., D'Hondt, S., 2012. Global distribution of microbial abundance and biomass in subseafloor sediment. Proceed. National Acad. Sci. 109 (40), 16213–16216.
Kay, S.M., Ramos, V.A., Dickinson, W.R., 2009. Backbone of the Americas: Shallow subduction, Plateau uplift, and Ridge and Terrane Collision, Vol. 204. Geological Society of America.
Kunz, J., Staudacher, T., Allegre, C.J., 1998. Plutonium-fission xenon found in Earth's mantle. Science 280 (5365), 877–880.
Labidi, J., Barry, P.H., Bekaert, D.V., Broadley, M.W., Marty, B., Giunta, T., Warr, O., Sherwood Lollar, B., Fischer, T.P., Avice, G., Caracausi, A., 2020. Hydrothermal 15N15N abundances constrain the origins of mantle nitrogen. Nature 580 (7803), 367–371.
Labidi, J., Young, E.D., Fischer, T.P., Barry, P.H., Ballentine, C.J., de Moor, J.M., 2021. Recycling of nitrogen and light noble gases in the Central American subduction zone: constraints from 15N15N. Earth Planet. Sci. Lett. 571, 117112.
Lages, J., Rizzo, A.L., Aiuppa, A., Robidoux, P., Aguilar Contreras, R., Apaza Choquehuayta, F.E. and Masías Alvarez, P.J., 2021. Crustal controls on light noble gas isotope variability along the Andean Volcanic Arc. *uri: issn: 2410339X*.
Magnabosco, C., Lin, L.H., Dong, H., Bomberg, M., Ghiorse, W., Stan-Lotter, H., Pedersen, K., Kieft, T.L., Van Heerden, E., Onstott, T.C., 2018. The biomass and biodiversity of the continental subsurface. Nat. Geosci. 11 (10), 707–717.
Marty, B., Contamine, D., Bekaert, D.V., Lastes, A., Pik, R., Labidi, J., Young, E.D., Broadley, M.W., Barry, P.H., Byrne, D.J., Seltzer, A.M., 2024. Uncovering the Xenon Isotope Composition of Continental Rift magmas: Insight from Analysis of Geothermal Gases At Homa Hills. EPSL, Kenya. In Review.
Matthews, S.J., Marquillas, R.A., Kemp, A.J., Grange, F.K., Gardeweg, M.C., 1996. Active skarn formation beneath Lascar Volcano, northern Chile: a petrographic and geochemical study of xenoliths in eruption products. J. Metamorphic Geol. 14 (4), 509–530.
McGlashan, N., Brown, L., Kay, S., 2008. Crustal thickness in the central Andes from teleseismically recorded depth phase precursors. Geophys. J. Int. 175 (3), 1013–1022.
Mook, W.G., Van Der Plicht, J., 1999. Reporting 14C activities and concentrations. Radiocarbon 41 (3), 227–239.
Newell, D.L., Jessup, M.J., Hilton, D.R., Shaw, C.A., Hughes, C.A., 2015. Mantle-derived helium in hot springs of the Cordillera Blanca, Peru: implications for mantle-to-crust fluid transfer in a flat-slab subduction setting. Chem. Geol. 417, 200–209.
Orcutt, B.N., Edwards, K.J., 2014. Life in the ocean crust: lessons from subseafloor laboratories. In: Developments in Marine Geology, 7. Elsevier, pp. 175–196.
Ozima, M., Podosek, F.A., 2002. Noble Gas Geochemistry. Cambridge University Press.
Perkins, J.P., Ward, K.M., de Silva, S.L., Zandt, G., Beck, S.L., Finnegan, N.J., 2016. Surface uplift in the Central Andes driven by growth of the Altiplano Puna Magma Body. Nat. Commun. 7 (1), 13185.
Porcelli, D., Ballentine, C.J., 2002. Models for distribution of terrestrial noble gases and evolution of the atmosphere. Rev. Mineral. Geochem. 47 (1), 411–480.
Profeta, L., Ducea, M.N., Chapman, J.B., Paterson, S.R., Gonzales, S.M.H., Kirsch, M., Petrescu, L., DeCelles, P.G., 2015. Quantifying crustal thickness over time in magmatic arcs. Sci. Rep. 5 (1), 17786.
Quade, J., Dettinger, M.P., Carrapa, B., DeCelles, P., Murray, K.E., Huntington, K.W., Cartwright, A., Canavan, R.R., Gehrels, G., Clementz, M., 2015. The growth of the central Andes, 22 S–26 S.
Ray, M.C., Hilton, D.R., Muñoz, J., Fischer, T.P., Shaw, A.M., 2009. The effects of volatile recycling, degassing and crustal contamination on the helium and carbon geochemistry of hydrothermal fluids from the Southern Volcanic Zone of Chile. Chem. Geol. 266 (1–2), 38–49.
Rogers, T.J., Buongiorno, J., Jessen, G.L., Schrenk, M.O., Fordyce, J.A., de Moor, J.M., Ramírez, C.J., Barry, P.H., Yücel, M., Selci, M., Cordone, A., 2023. Chemolithoautotroph distributions across the subsurface of a convergent margin. ISME J. 17 (1), 140–150.
Salisbury, M.J., 2011. Convergent Margin Magmatism in the Central Andes and Its Near Antipodes in Western Indonesia: Spatiotemporal and Geochemical Considerations. Oregon State University.
Sano, Y., Marty, B., 1995. Origin of carbon in fumarolic gas from island arcs. Chem. Geol. 119 (1–4), 265–274.
Seltzer, A.M., Bekaert, D.V., 2022. A unified method for measuring noble gas isotope ratios in air, water, and volcanic gases via dynamic mass spectrometry. Int. J. Mass spectrom. 478, 116873.
Stern, C.R., 2004. Active Andean volcanism: its geologic and tectonic setting. Revista Geológica de Chile 31 (2), 161–206.
Stuiver, M., Polach, H.A., 1977. Discussion reporting of 14C data. Radiocarbon 19 (3), 355–363.
Summit, M., Baross, J.A., 2001. A novel microbial habitat in the mid-ocean ridge subseafloor. Proceed. National Acad. Sci. 98 (5), 2158–2163.
Syracuse, E.M., Abers, G.A., 2006. Global compilation of variations in slab depth beneath arc volcanoes and implications. Geochem., Geophys., Geosystems 7 (5).
Tassi, E.L., Pedron, F., Barbafieri, M., 2011. Evaluating the absorption of boron by plants—A potential tool to remediate contaminated sediments from Cecina River Basin in Italy. Water, Air, & Soil Pollution 216, 275–287.
Ward, K.M., Zandt, G., Beck, S.L., Christensen, D.H., McFarlin, H., 2014. Seismic imaging of the magmatic underpinnings beneath the Altiplano-Puna volcanic complex from the joint inversion of surface wave dispersion and receiver functions. Earth Planet. Sci. Lett. 404, 43–53.
Xu, Y., Li, X., Luo, M., Xiao, W., Fang, J., Rashid, H., Peng, Y., Li, W., Wenzhöfer, F., Rowden, A.A., Glud, R.N., 2021. Distribution, source, and burial of sedimentary organic carbon in Kermadec and Atacama Trenches. Journal of Geophysical Research: Biogeosciences 126 (5) e2020JG006189.
Young, E.D., Rumble III, D., Freedman, P., Mills, M., 2016. A large-radius high-mass-resolution multiple-collector isotope ratio mass spectrometer for analysis of rare isotopologues of O2, N2, CH4 and other gases. Int. J. Mass spectrom. 401, 1–10.
Yeung, L.Y., Li, S., Kohl, I.E., Haslun, J.A., Ostrom, N.E., Hu, H., Fischer, T.P., Schauble, E.A., Young, E.D., 2017. Extreme enrichment in atmospheric 15N15N. Sci. Adv. 3 (11), eaao6741.